Geophysical Journal International

Geophys. J. Int. (2015) **203,** 1302–1318 doi: 10.1093/gji/ggv368
GJI Seismology

Ultra-low velocity zones beneath the Philippine and Tasman Seas revealed by a trans-dimensional Bayesian waveform inversion

Surya Pachhai,[1] Jan Dettmer[1,2] and Hrvoje Tkalčić[1]

[1]*Research School of Earth Sciences, The Australian National University, Canberra, Australia. E-mail: Surya.Pachhai@anu.edu.au*
[2]*School of Earth and Ocean Sciences, University of Victoria, Victoria, BC, Canada*

Accepted 2015 September 2. Received 2015 August 26; in original form 2015 April 10

SUMMARY

Ultra-low velocity zones (ULVZs) are small-scale structures in the Earth's lowermost mantle inferred from the analysis of seismological observations. These structures exhibit a strong decrease in compressional (*P*)-wave velocity, shear (*S*)-wave velocity, and an increase in density. Quantifying the elastic properties of ULVZs is crucial for understanding their physical origin, which has been hypothesized either as partial melting, iron enrichment, or a combination of the two. Possible disambiguation of these hypotheses can lead to a better understanding of the dynamic processes of the lowermost mantle, such as, percolation, stirring and thermo-chemical convection. To date, ULVZs have been predominantly studied by forward waveform modelling of seismic waves that sample the core–mantle boundary region. However, ULVZ parameters (i.e. velocity, density, and vertical and lateral extent) obtained through forward modelling are poorly constrained because inferring Earth structure from seismic observations is a non-linear inverse problem with inherent non-uniqueness. To address these issues, we developed a trans-dimensional hierarchical Bayesian inversion that enables rigorous estimation of ULVZ parameter values and their uncertainties, including the effects of model selection. The model selection includes treating the number of layers and the vertical extent of the ULVZ as unknowns. The posterior probability density (solution to the inverse problem) of the ULVZ parameters is estimated by reversible jump Markov chain Monte Carlo sampling that employs parallel tempering to improve efficiency/convergence. First, we apply our method to study the resolution of complex ULVZ structure (including gradually varying structure) by probabilistically inverting simulated noisy waveforms. Then, two data sets sampling the CMB beneath the Philippine and Tasman Seas are considered in the inversion. Our results indicate that both ULVZs are more complex than previously suggested. For the Philippine Sea data, we find a strong decrease in *S*-wave velocity, which indicates the presence of iron-rich material, albeit this result is accompanied with larger parameter uncertainties than in a previous study. For the Tasman Sea data, our analysis yields a well-constrained *S*-wave velocity that gradually decreases with depth. We conclude that this ULVZ represents a partial melt of iron-enriched material with higher melt content near its bottom.

Key words: Probability distributions; Mantle processes; Composition of the mantle; Body waves; Seismic tomography; Computational seismology.

1 INTRODUCTION AND MOTIVATION

1.1 Lowermost mantle heterogeneities

The core–mantle boundary (CMB) is located at ∼2900 km depth and separates two fundamentally distinct structures and dynamic regimes of the Earth's interior. The core is composed of a metallic alloy consisting of mostly iron and nickel, and some lighter elements (e.g. oxygen, carbon, potassium and silicon) while the mantle is largely composed of silicates and oxide minerals (e.g. Ringwood 1979; Ringwood & Hibberson 1991). Based on 1-D earth models, the absolute density contrast at the CMB is ∼4500 kg m^{-3} (e.g. ak135, Kennett *et al.* 1995), exceeding that at the Earth surface. This density contrast provides favourable conditions for the formation of chemical heterogeneities or density stratification near the CMB (Young & Lay 1987).

The lowermost mantle region has been extensively studied using various seismological observations and methods, which led to the discovery of increasingly complex structure. The lowermost mantle complexities include heterogeneities at various length-scales

(e.g. Doornbos 1974; Haddon & Cleary 1974; Masters *et al.* 1996; Wysession 1996; Wysession *et al.* 1999; Bréger *et al.* 2000; Tkalčić *et al.* 2002; Tkalčić & Romanowicz 2002; Rost & Earle 2010), the existence of pronounced topography (e.g. Lay & Helmberger 1983; Thomas *et al.* 2004; Tanaka 2010; Soldati *et al.* 2012), strong anisotropy (e.g. Lay *et al.* 1998; Garnero *et al.* 2004; Wenk *et al.* 2011) and the existence of multiscale (both short- and long-wavelength) heterogeneities (Young *et al.* 2013).

The complexities of particular interest in this study are localized and thin zones (as thin as 3.5 km) of strong negative seismic velocity anomalies known as ultra-low velocity zones (ULVZs, e.g. Garnero & Helmberger 1995, 1998; Williams & Garnero 1996). The ULVZs are small-scale (lateral and vertical) velocity and density anomalies at the top of the CMB, where the seismic wave velocity can be reduced by more than 10 per cent with respect to 1-D reference models.

1.2 Seismological ULVZ studies and their implications

Locations and elastic properties of ULVZs were first studied with travel time anomaly data and forward waveform modelling of SPdKS waves (*S* waves converted to diffracted *P* waves along the mantle side of the CMB, and converted back to *S* waves upon exit from the outer core; Garnero & Helmberger 1995, 1996). These studies suggest a reduction in *P*-wave velocity of up to 10 per cent. Thereafter, SPdKS waves were extensively analysed to constrain ULVZ parameters and their lateral variability (e.g. Garnero & Helmberger 1995, 1996; Helmberger *et al.* 1998; Wen & Helmberger 1998a,b). Recent studies suggest a larger decrease in *P*-wave velocity. For example, Thorne *et al.* (2013) propose at a >15 per cent decrease in *P*-wave velocity while Brown *et al.* (2015) find a decrease in *P*-wave velocity of up to 23 per cent. However, SPdKS waves cannot uniquely constrain ULVZ locations and parameters due to the ambiguity between anomalous structures located at either the source- or receiver-side of the CMB. Some studies also applied 2-D modelling of SPdKS waves to constrain the vertical and lateral extent of ULVZ structures (e.g. Wen & Helmberger 1998a,b; Helmberger *et al.* 2000; Rondenay *et al.* 2010; To *et al.* 2011; Jensen *et al.* 2013; Thorne *et al.* 2013). Note that, 2-D modelling also suffers from the source-/receiver-side ambiguity and can add an additional trade-off (strong and laterally narrow ULVZ vs. a weak and laterally large ULVZ). Array analysis (e.g. velocity-spectral and frequency–wavenumber analysis) and cross-path ray geometry can be used to remove such ambiguity and estimate the location of the ULVZ (Rondenay & Fischer 2003; Thorne & Garnero 2004). However, array analysis may not uniquely quantify the ULVZ parameters if such structure exists on both the source and receiver side of the CMB while the cross-path geometry is limited due to the earthquake source and receiver geometry.

In contrast to SPdKS waves, the use of PcP (*P* wave reflected at the CMB) and ScP (*S* wave reflected, at the CMB, and converted to *P*) waves (Fig. 1a) remove source- and receiver-side ambiguity and plays a key role in studying ULVZs. The core reflected waves become complex due to wave conversions at interfaces within the ULVZ, which results in pre- and post-cursors (signals that arrive before and after the CMB arrival, respectively; see Figs 1c and d). The amplitudes and positions of pre- and post-cursors depend on the anomalous velocity and density structure including vertical and lateral extent. Additionally, the position of ULVZs relative to the ScP bouncing points on the CMB is also relevant to the interpretation of results. For example, Brown *et al.* (2015) demonstrate that large ScsP post-cursors (*S* waves reflected as *S* waves from the CMB and subsequently converted to *P* waves at the upper ULVZ boundary) can be generated without precursors when *S* waves are not directly incident on the ULVZ. Signals reflected at the top of ULVZs, particularly for interfaces with weak impedance contrast, are difficult to detect in the presence of noise. The deployment of seismic arrays plays an important role to enhance weak signals by stacking. Stacking enhances the coherent signal, which is distinct from incoherent noise due to its amplitude and waveform (e.g. Rost & Thomas 2002; Rost & Thomas 2009). The study of complex stacked waveforms can constrain ULVZ parameters and has been extensively carried out via forward modelling (e.g. Rost *et al.* 2005; Idehara *et al.* 2007; Idehara 2011).

The ULVZ parameters estimated from inversion of seismological observations are linked to variations in composition, temperature, and phase at deep mantle temperature (∼2500 K) and pressure (∼120 GPa) conditions using mineralogical experiments. Based on these experiments, two main physical mechanisms have been put forward to explain the origin of ULVZs: Iron enrichment (e.g. Knittle & Jeanloz 1991; Manga & Jeanloz 1996) and partial melting in the lowermost mantle (e.g. Williams & Garnero 1996; Berryman 2000). Different sources for the mechanism of iron enrichment have been proposed. For example, the residue of a fractional crystallization of a primordial magma ocean (Labrosse *et al.* 2007), a chemically distinct layer of a banded form of iron subducted by a slab (Dobson & Brodholt 2005), and blobs of iron-rich liquid originated from the core due to morphological instability at the CMB (Otsuka & Karato 2012). Additionally, Mao *et al.* (2006) suggest that iron-rich silicate can account for the anomalous properties of ULVZs. However, the origin of the iron in perovskite mineral and its stability at the base of the mantle is debated and Zhang *et al.* (2014) showed that the perovskite could lose the iron to other mineral phases at the lowermost mantle pressure and temperature conditions.

The second mechanism proposed as the cause of the seismic velocity anomalies is partial melting of the lowermost mantle. The approximate 3:1 ratio of *S*-wave velocity to *P*-wave velocity perturbations in the ULVZ is generally argued to be of partial melt origin (e.g. Williams & Garnero 1996; Revenaugh & Meyer 1997; Garnero *et al.* 1998). A partial melting origin is also proposed based on studies of the correlation of ULVZ locations and hotspot locations at the Earth surface (e.g. Williams *et al.* 1998). In addition, a decrease in *P*-wave velocity of up to 10 per cent can be explained by a fraction of 5–30 per cent of melt depending on the melt geometry (e.g. Williams & Garnero 1996; Williams *et al.* 1998). However, remaining questions concern the complexity of the melt geometry and the uncertainties of the temperature estimates at the CMB. Therefore, quantification of ULVZ parameters and their uncertainties is desirable to help in the interpretation of the physical origin of the ULVZs. To this end, this work aims to provide the most rigorous study of ULVZ parameters and their uncertainties through a probabilistic (Bayesian) inversion of ScP waveforms to date.

1.3 Seismological inference of ULVZ parameters

In forward modelling, data are predicted for various sets of ULVZ parameter values (layering, densities, velocities, Fig. 1b) and data predictions are compared to the observed data in a trial-and-error approach. However, the strong non-uniqueness of the inverse problem (parameter trade-offs) often causes ambiguous interpretation (e.g. Garnero & Helmberger 1998; Pachhai *et al.* 2014). While many studies (e.g. Helmberger *et al.* 1998; Rost *et al.* 2006;

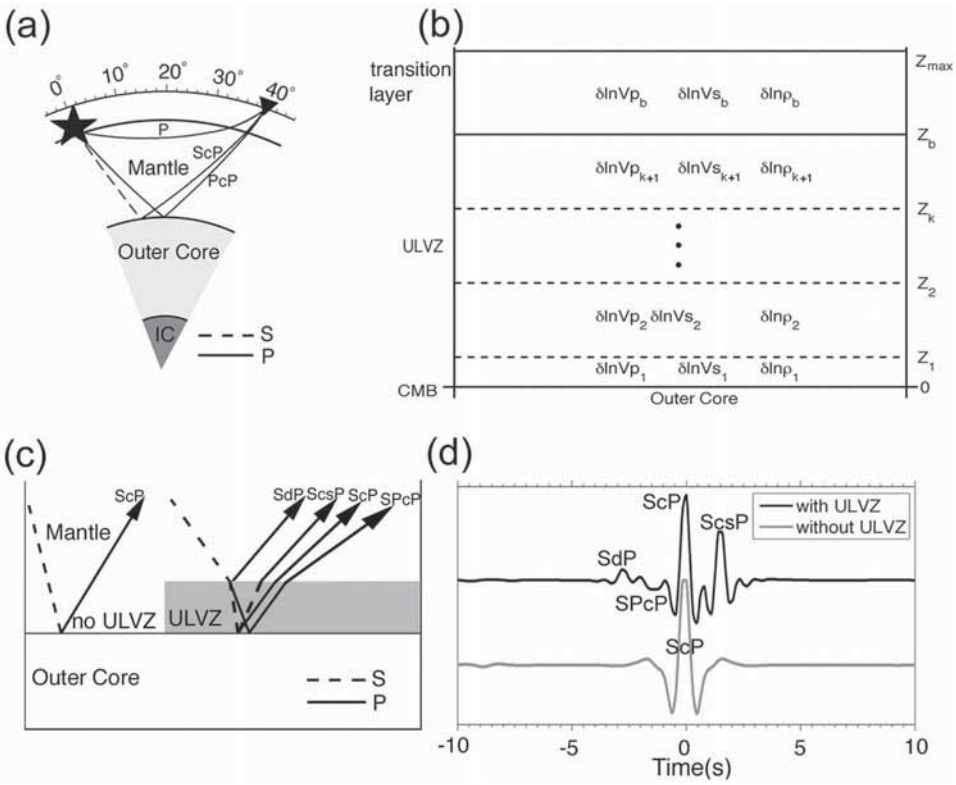

Figure 1. (a) Geometric ray paths for PcP and ScP waves at an epicentral distance 40°, earthquake source location (star), and receiver location (triangle). (b) Model parametrization of the earth model for ULVZ layers on the top of the CMB. Parameters are defined in the text. *k* and *b* denote the interface and transition layer index. Horizontal dashed lines are interfaces. (c) Schematic diagram of a 1-D, one-layer ULVZ on the top of the CMB and its effect on the ScP wave. (d) The ScP wave and its converted phases due to 1-D ULVZ structure (black) and without ULVZ (grey). Phases due to conversion at ULVZ layer are marked as SdP, SPcP, ScP and ScsP. All waveforms are normalized and centred on the maximum amplitude.

Idehara 2011) perform sensitivity analysis for ULVZ parameters and find a single model to provide optimal values (considering only a single set of parameter values as the solution to the inverse problem), some recent work has included grid search (e.g. Rost *et al.* 2005; Hutko *et al.* 2009). However, such methods are limited to the sampling of models with few parameters and optimal models do not consider other solutions that may also fit the data reasonably well. In addition, choosing only a single parametrization (e.g. a 1-layer ULVZ) results in strong dependence of the inversion results on that parametrization choice (e.g. Dettmer *et al.* 2009). Furthermore, ULVZ parameter estimates can be uncertain due to the effects of measurement errors (due to the data recording process) and theory errors (e.g. model parametrization simplifications, assumptions in the data processing). The uncertainty estimation quantifies the accuracy of the particular model adopted to represent the structure. Therefore, optimal solutions cannot capture the full data information.

An important, but to date rarely studied, aspect of ULVZ parameter estimation is to quantify parameter uncertainties and distinguish uncertainty from parameter variability as a function of ULVZ height above the CMB as well as a function between various sites (variability is a measure of difference in structure while uncertainty is a measure of our knowledge of structure). A Bayesian formulation of the inverse problem (e.g. Tarantola 2005; Sambridge & Moseguard 2002) can rigorously quantify parameter estimates and uncertainties for non-linear and non-unique problems such as waveform inversion. In Bayesian inversion, unknown parameters are considered to be random variables and probabilities are used to express degrees of belief that a parameter value is consistent with reality. The posterior probability density (PPD, solution to the inverse problem) of the parameters combines prior information (independent of the data) with data information (expressed by the likelihood function). The likelihood function is defined by assuming a statistical distribution type for data errors (e.g. Gaussian) while the parameters of that distribution are often estimated from the data together with the geophysical parameters. The high-dimensional PPD is typically interpreted by computing marginal densities and other moments (e.g. averages, standard deviations) of the PPD.

Pachhai *et al.* (2014) developed a Bayesian inversion for ULVZ parameters where an optimal parametrization was considered. The ULVZ was parametrized by flat-lying, homogeneous layers extending from the CMB upwards to a maximum height. Note that for observed data, the number of layers is unknown and should not be fixed to a subjective number, but rather be estimated from the data. This model selection is particularly important when uncertainties are of interest since too complex parametrizations cause overfitting of data resulting in overestimated uncertainties and too simple parametrizations underfit data resulting in underestimated uncertainties. Pachhai *et al.* (2014) apply the Bayesian information criterion (BIC, Schwarz 1978) to identify the optimal number of interfaces. The BIC identified a two-layer ULVZ model as optimal. This model exhibits a strong decrease in *S*-wave velocity and a strong gradual increase in density as a function of depth. While the BIC approach is practical and provides quantitative uncertainty analysis, it is based on an approximation of the posterior as a multivariate Gaussian around the maximum likelihood vector (which causes limitations for posteriors with multiple modes of similar likelihood), can be tedious to apply, and does not include the effect

of parametrization uncertainty in the uncertainty estimation (i.e. multiple parametrizations may explain the data reasonably well and should be considered simultaneously/integrated over).

This paper applies trans-dimensional (trans-D) Bayesian inversion to address the uncertain parametrization (Malinverno 2002; Sambridge *et al.* 2006). Trans-D inversion relaxes the requirement of specifying a single parametrization to a variable model parametrization that simultaneously considers models with differing numbers of layers. The resulting PPD includes model selection uncertainty and is considered to be more meaningful. Trans-D inversion is widely applied to study Earth structure (e.g. Bodin & Sambridge 2009; Agostinetti & Malinverno 2010; Dettmer *et al.* 2010; Minsley 2011; Young *et al.* 2013) and dynamics (e.g. Tkalčić *et al.* 2013). The sampling is performed here using reversible jump Markov chain Monte Carlo (rjMCMC, Green 1995) which generalizes the Metropolis-Hasting acceptance rule to allow jumps between models which are implemented by a birth-death scheme (Geyer & Møller 1994; Denison *et al.* 2002). In addition to trans-D layer sampling, a trans-D first order autoregressive (AR1) error model is included in the inversion to address correlated data errors (Steininger *et al.* 2013). The trans-D AR1 sampling provides an efficient data-driven process to probabilistically include the AR1 coefficient only when required by the data and to avoid both under- and overparametrization of the error model.

Metropolis–Hastings (MH) sampling can be inefficient for strongly nonlinear problems, particularly when extensive low probability regions separate multiple high probability modes or when the model is trans-D (MacKay 2003). In such cases, MH sampling can take extremely long times to transition between modes, resulting in poor and sometimes prohibiting convergence. Interacting Markov chains (parallel tempering, e.g. Geyer 1991; Dettmer & Dosso 2012) are applied here to provide more efficient sampling.

First, our method is applied to simulated ScP waveforms that sample complex 1-D structure with a gradual decrease in *P*- and *S*-wave velocity and an increase in density within the top and bottom 3 km of the ULVZ. The trans-D inversion recovers the complex structure with a gradual increase in parameter perturbations reasonably well on the top of the ULVZ, even after adding correlated noise, and shows the ability of the inversion to recover complex ULVZs. However, the inversion can recover such structure at the bottom only if the impedance contrast is strong enough to change the shape of the waveform. The inversion is then applied to two sets of observed ScP waveforms sensitive to the CMB beneath the Philippine Sea and the CMB beneath the Tasman Sea (east of Australia). We note that the Philippine Sea data was previously studied (Pachhai *et al.* 2014) and is included here to examine the performance of the trans-D inversion approach. The Philippine trans-D results confirm a ULVZ with a strong *S*-wave velocity anomaly. The parameter uncertainty (including interface height) is larger compared to previous results which is consistent with the more general uncertainty estimates expected from trans-D inversion. The larger uncertainties reduce resolution of meaningful *P*-wave velocity and density layering. Hence, the new result favours an iron enriched lowermost mantle. In contrast, results for the Tasman Sea data suggest a strong *S*-wave velocity perturbation with a gradual increase as a function of depth which can be interpreted as more melt material near the bottom of the zone. In both regions, it is challenging to clearly differentiate between the two origins (partial melting and iron enrichment) due to significant uncertainties in *P*-wave velocity and density. However, the results clearly show different types of ULVZs at the two locations. The differences could be a result of different shapes and morphologies of the two ULVZs.

2 INVERSION METHOD

This section summarizes the inversion method developed here for the study of ULVZs. For more details about this approach and our particular implementation, we refer readers to, for example, Malinverno (2002), Sambridge *et al.* (2006) and Dettmer *et al.* (2013).

2.1 Trans-dimensional Bayesian inversion

In Bayesian inversion, the solution to an inverse problem is given by the posterior probability density (PPD). Probability densities are expressed in terms of conditional probabilities and indicated by |. For example, the conditional probability of **x** given **y** is expressed as $p(\mathbf{x}|\mathbf{y})$. For a vector of N measured data **d** and a vector of M model parameters **m**, Bayes' theorem for a trans-D model can be expressed as (Green 1995)

$$p\,(k, \mathbf{m}_k|\mathbf{d}) = \frac{p\,(k)\,p\,(\mathbf{d}|k, \mathbf{m}_k)\,p\,(\mathbf{m}_k|k)}{\sum_{k'} \int p\,(k')\,p\,(\mathbf{d}|k', \mathbf{m}'_{k'})\,p\,(\mathbf{m}'_{k'}|k')\;d\mathbf{m}'_{k'}}, \tag{1}$$

where k is the model index (i.e. the number of interfaces or layers), $p(k)$ is the prior probability of the number of interfaces, $p(\mathbf{m}_k|k)$ is the prior for the elastic parameters for a given interface and $p(k, \mathbf{m}_k|\mathbf{d})$ is the PPD defined over the trans-D model space. The term in the denominator is the total evidence of all models indexed by k and is difficult to evaluate. Note that for relative inference in a group of models, the evidence does not need to be computed. Therefore, the hierarchical form of eq. (1) constitutes an efficient approach to Bayesian model selection. For observed (fixed) data, $p(\mathbf{d}|k, \mathbf{m}_k)$ represents the likelihood of the model and is written as $L(k, \mathbf{m}_k)$ (a function of only k and **m**).

The likelihood function is derived by assuming a statistical distribution form for data errors. Generally, data errors are not directly accessible in the inverse problem and must be approximated by residual errors that combine both measurement errors (as a result of the measurement process) and theory errors (e.g. resulting from model and signal processing approximations). Here, we assume Gaussian data errors and account for correlated errors by applying an autoregressive process of order 1 (AR1), for details see Dettmer *et al.* (2012) and Steininger *et al.* (2013). In that case, the likelihood function can be formulated as

$$L(k, \mathbf{m}_k) = \frac{1}{\sqrt{(2\pi)^N \sigma^N}} \exp\left[-\frac{1}{2\sigma^2}\left|\left(\mathbf{d}^{\text{obs}} - \mathbf{d}\,(k, \mathbf{m}_k) - \mathbf{d}\,(\mathbf{a})\right)\right|^2\right], \tag{2}$$

where $\mathbf{d}(\mathbf{a})$ are AR1 predictions for AR1 parameters **a**, which account for serial correlation. Here, the standard deviation of the residual errors (σ) and the AR1 coefficient are treated as unknowns.

2.2 Prior information

The prior includes information about the model parameters that is independent from the data. For the trans-D partition models, the prior is the product of the prior for the number of interfaces $p(k)$, the prior for the interface height given the number of interfaces $p(\mathbf{z}_k|k)$, the prior for the transition layer parameters given the number of interfaces, the prior for the ULVZ parameters, and the prior for the standard deviation and correlation of the data errors. The priors for the ULVZ parameters (interface height, velocity and density perturbations), transition layer parameters (interface height, velocity and density perturbations), and standard deviation and correlation coefficients of data errors are expressed in terms of uniform

distributions over physically meaningful bounds. However, $p(\mathbf{z}_k|k)$ requires more careful consideration.

In most geophysical applications to date, the model is parametrized such that the prior $p(k)$ is defined over a fixed depth interval and priors for all layer parameters are identical. In that case, the prior $p(\mathbf{z}_k|k)$ is expressed in terms of the 'grid trick' (e.g. Denison *et al.* 2002). The grid trick temporarily assumes a fictitious discretization with a discrete set of possible partition locations for k interfaces given by n choose k (the grid assumption cancels when the acceptance probability is derived). However, this approach is not satisfactory here since the ULVZ is inserted into a background whole-earth model (ak135). To achieve this parametrization we assume that the ULVZ can exist from the CMB upwards to some maximum height z_b. The simplest case, where no ULVZ is present, is achieved by considering the number of interfaces from the CMB to z_b as zero ($k = 0$) and $z_b = 0$. In this case we are still required to specify the elastic parameters from z_b to $z_{\max}$as random variables which we achieve by assuming narrow prior bounds for these parameters (to express strong prior preference for the ak135 parameters). We refer to this layer as the transition layer. The extent of the trans-D partition z_b is unknown with a uniform prior over $[0, z_{\max}]$. The transition layer is always present (akin to a semi-infinite half-space) from z_b to $z_{\max}$.

To consider z_b as unknown, we follow the parametrization approach of Steininger *et al.* (2013) and divide the model into two regions: A ULVZ and the transition layer. In the ULVZ region, flat-lying, homogeneous layers are added above the ScP-wave reflection points (representing the ScP Fresnel zone) and such layers are represented by a series of $k + 1$ layers with k interfaces. The topmost $(k + 1)$ ULVZ layer is defined by an unknown movable discontinuity z_b that separates the ULVZ from the transition region (Fig. 1b). That is to say, the vertical extent of the trans-D ULVZ model is an unknown parameter. In this parametrization, the prior for the ULVZ partition can be calculated separately using a Dirichlet distribution and be expressed as $p\,(\mathbf{z}_k|k) = (k-1)!z_b^{k-1}$. In this derivation, we assume that the concentration parameter is 1 to give equal probabilities to all interfaces. This shows how the priors on ULVZ interface height given the interface changes with the position of z_b. For a complete derivation of the Dirichlet prior, we refer Dosso *et al.* (2014).

2.3 Sampling approach

For non-linear inverse problems such as waveform inversion, no analytical solution exists for the PPD and reversible jump Markov chain Monte Carlo (rjMCMC) sampling is applied here to sample the PPD numerically. In rjMCMC sampling, the Markov chain must be able to transition (jump) between models with different parameter dimensions/meanings without violating detailed balance. If $q(k', \mathbf{m}'_{k'}|k, \mathbf{m}_k)$ is the distribution for a proposed transition from the current model $(k, \mathbf{m}_k)$ to a new model $(k', \mathbf{m}'_{k'})$, the proposed model is accepted/rejected with probability $\boldsymbol{\alpha}$ (Green 1995, 2003)

$$\alpha = \min\left[1, \frac{p\,(k', \mathbf{m}'_{k'})}{p\,(k, \mathbf{m}_k)}\left(\frac{L\,(k', \mathbf{m}'_{k'})}{L\,(k, \mathbf{m}_k)}\right)^{\beta}\frac{q\,(k, \mathbf{m}_k|k', \mathbf{m}'_{k'})}{q\,(k', \mathbf{m}'_{k'}|k, \mathbf{m}_k)}|\mathbf{J}|\right], \tag{3}$$

where $|\mathbf{J}|$ is the determinant of the Jacobian matrix (in this implementation, $|\mathbf{J}|$ equals unity) and β is the tempering parameter used for parallel tempering. In this scheme, lower values of β decrease the likelihood function in eq. (3) resulting in wider exploration of the parameter space while chains with high β-values preferentially sample high posterior probability regions. Parameter inferences are based on chains with $\beta = 1$ that provide unbiased samples from the PPD. Moreover, parameters from randomly selected chain pairs are exchanged based on the MH acceptance which allows the algorithm to take advantage of the various ranges of exploration scales without biasing the PPD (e.g. Dettmer & Dosso 2012).

The rjMCMC algorithm applies the birth/death scheme (e.g. Geyer & Møller 1994) to sample models from 0 to 4 interfaces. For birth moves, a new interface is created at a random position between the CMB and z_b. Then one of the two new layers is randomly picked and new parameter values are drawn from the uniform prior. For a death move, a random interface is deleted and the parameters for that layer are deleted. Perturbation moves are applied to perturb layer parameters without changing the model dimension.

3 FORWARD MODELLING AND RESOLUTION STUDY

This section presents a forward model required for Bayesian inversion of ScP waveforms followed by a number of synthetic experiments to show the ability of the inversion to constrain the ULVZ structures and their complexities.

3.1 Forward model

Nonlinear Bayesian inversion requires a large number of earth models to be perturbed and waveforms to be computed. The ak135 model (Kennett *et al.* 1995) provides the background model, which is refined by including the trans-dimensional model with a varying number of horizontal, and laterally homogeneous layers above the CMB. The computational cost limits the algorithm choice for computing synthetic seismograms. Therefore, the computationally efficient Wentzel, Kramers, Brillouin and Jeffreys (WKBJ) method (Chapman & Orcutt 1985) is applied here.

The synthetic seismograms are computed in the following steps: (i) Green functions are computed by WKBJ and convolved with the moment rate function (Brüstle & Müller 1983), which is computed for a pulse width equal to that of the observed PcP wave; (ii) a narrow band-pass filter (corner frequencies of 0.5–1.5 Hz) is applied in a long time window (60 s) so that the middle section remains unaffected by any filtering artefacts; (iii) a final synthetic seismogram is obtained by deconvolving the PcP waveform from the ScP waveform. This last step is applied to remove the source and path effects assuming that the PcP wave does not sample the ULVZ. This assumption is consistent with the data processing where complex PcP waves (suspected of sampling the ULVZ) are not considered in the analysis. Upsampling by a factor of 10 is applied before the cross-correlation between the observed and predicted waveforms to ensure accurate peak alignment (crucial to obtain meaningful likelihood values).

3.2 Feasibility and parameter resolution study

This section presents a series of simulations to study resolution ability of trans-D ScP waveform inversion with regard to thin and complex ULVZ features. In particular, we aim to address several questions currently present in the literature due to limitation of the existing seismological methods and sensitivities of various seismological data types. One of the controversies is the distribution of ULVZs at some CMB locations since undetected ULVZs are overlapped/juxtaposed with detected ULVZs. For example, a past study (Thorne & Garnero 2004) infers ULVZs in a wide region of the CMB beneath the western Pacific using forward modelling of

SPdKS waveforms. However, some other studies (e.g. Rost *et al.* 2005; Rost *et al.* 2006; Idehara *et al.* 2007) do not detect the ULVZs in some places of the same region using modelling of short-period ScP and PcP waveforms.

A further example of disagreement is on the vertical resolution of core-reflected waves (ScP and PcP). Some studies (Rost & Revenaugh 2003; Rost *et al.* 2010b) demonstrate that forward modelling of ScP and PcP waveforms can detect ULVZs as thin as ∼5 km with strong velocity and density anomalies. Another study, using total variation deconvolution of synthetic data, demonstrates that the vertical resolution of ScP waveforms is ∼3 km (Rost *et al.* 2010a). Similarly, Idehara (2011) is able to detect ULVZs as thin as ∼4.0 km by applying waveform modelling of deconvolved ScP waveforms. Finally, array analysis of ScP waveforms indicates that the vertical resolution is ∼7 km (Rost *et al.* 2010a). This is because the precursor due to the reflection from the top of a 7-km-thick layer is hardly visible just before the main pulse of the ScP waveform.

In addition to these controversies in vertical resolution of a single-layer ULVZs and their locations, there are a few other studies which indicate the presence of multiple-layer ULVZs. For example, Thybo *et al.* (2003) infers a two-layer ULVZ with gradual decrease in *P*-wave velocity, *S*-wave velocity, and an increase in density as a function of depth utilizing the waveform modelling of PcP waveforms sampling the CMB beneath Siberia. They suggest a top ULVZ layer is as thin as ∼1.2 km while the bottom layer as ∼6.0 km. Their interpretation for such structure is that it is due to partial melting of iron-enriched material in the lowermost mantle with dense melt-rich material near the bottom of the ULVZ. Similarly, Idehara (2011) infers two-layer ULVZs beneath the Philippine Sea with dense material on top of less dense material. For the same data, Pachhai *et al.* (2014) also find a complex 2-layer structure while an even more complex ULVZ with an additional layer sandwiched between the two layers is rejected by model selection based on the BIC.

To examine the resolution of layer thickness for various impedance contrasts, we invert several simulated noisy ScP waveforms. We begin with simulations for two different structures: A gradual increase in velocity and density perturbations limited to (1) the top 3 km of the ULVZ and (2) the bottom of the ULVZ. This will be followed by an inversion for structure with a sandwiched layer.

In all cases, we assume that the PcP wave does not sample the ULVZ and is used to remove the effects of source and mantle structure by deconvolving it from the ScP wave. If this assumption is correct, it follows that any complexity seen in the deconvolved ScP-waveform is due to the presence of a ULVZ. Additionally, the measured data typically show strong serial correlation in the residual errors (Pachhai *et al.* 2014). To address these correlations, a first order autoregressive error model (AR1 coefficient of 0.5) with Gaussian random errors of standard deviation $\sigma = 0.02$ m s^{-1} (2 per cent of the amplitude of the wave) is applied to simulate correlated errors. The correlated errors are added to the deconvolved ScP-waveform to produce the simulated data for the resolution tests.

3.2.1 *Increased complexity at the top of the ULVZ*

Our goal in this experiment is to estimate the resolution power of our method by gradually increasing the complexity within the top 3 km of the ULVZ. Note that all simulated inversions are trans-D (the number of layers is unknown) and hierarchical (noise parameters are unknown). This approach results in more reasonable (larger) uncertainty estimates and is advantageous since no decision about the number of layers resolved by the data has to be based on independent information/reasoning. Only one result for the noise will be shown because the same values of noise parameters are applied in all cases.

In the first simulation, we consider an ScP waveform that samples a ULVZ of 10-km height with a 10 per cent decrease in *P*-wave velocity, a 25 per cent decrease in *S*-wave velocity, and a 19 per cent increase in density. Above 10-km height, the model is consistent with the ambient mantle and the model parameter values characterizing the perturbation in elastic properties are set to zero for that zone. The deconvolved ScP-waveforms with and without noise are shown in Fig. 2. The prior widths for the ULVZ layers are given by the axis limits in the figures for posterior profile marginals (e.g. Fig. 2). The inversion for the simulated data also includes the trans-D autoregressive error model to account for the residual correlations that are added to the data. The priors for standard deviation and the AR1 coefficient are from 0.0 to 0.2, and −0.5 to 0.99, respectively. The inversion is initialized with an arbitrary model (not the true model) in each of 35 chains with the logarithmic spacing of the tempering levels set to 1.35. All parallel tempering chains are repeatedly refocused on the best model during burn-in and after that only one chain ($\beta = 1$) collects samples. The likelihood values are computed in a 20-s window around the central peak. The first third of the PPD samples are discarded as burn-in (ensuring that the sampling is not biased by the starting model and excluding all resets). Samples after the burn-in period are considered for parameter inference. We monitor the convergence of the algorithm by examining the sampling history for various parameters by comparing inferences for the first third of PPD samples (post burn-in) to inferences for the last third. When no significant differences exist in the marginals of parameters, the sampling is considered to have converged.

The right-hand column of Fig. 2(a) shows the inversion results in terms of profile marginal densities for different ULVZ parameters. Profile marginal densities are obtained by considering only the parameter of interest as a function of height above the CMB while integrating out all other parameters in the PPD. In this process, the height above the CMB is discretized and we choose to normalize each depth interval individually. Hence, the profile marginals combine the results of the various parametrizations simultaneously considered in the trans-D inversion. The *S*-wave velocity is slightly underestimated, but within the uncertainty limit while other parameters are estimated well. In addition, the inversion clearly estimates the true interface at 10 km. The uncertainties of *P*-wave velocity, *S*-wave velocity, and density are approximately ±4, ±2 and ±5 per cent, respectively.

The second simulation includes a ULVZ of two closely spaced interfaces with gradual decrease in velocity and an increase in density. The bottom layer is 8 km thick while the top layer is 2 km thick. This ULVZ has the same properties in the bottom layer as the ULVZ from the first simulation. The *P*-wave velocity, *S*-wave velocity and density perturbations for the top layer are −6, −21 and 12 per cent, respectively. The simulated data with and without noise are shown in Fig. 2(b). The amplitudes of the precursors decrease and broaden in comparison with those from the previous case because of the gradual changes in velocities and density. Fig. 2(b) also shows the inversion results in terms of profile marginal densities for different ULVZ parameters. The inversion recovers all model parameters of the top layer including the interface height (10 km). However, while the true values still lie within the uncertainty

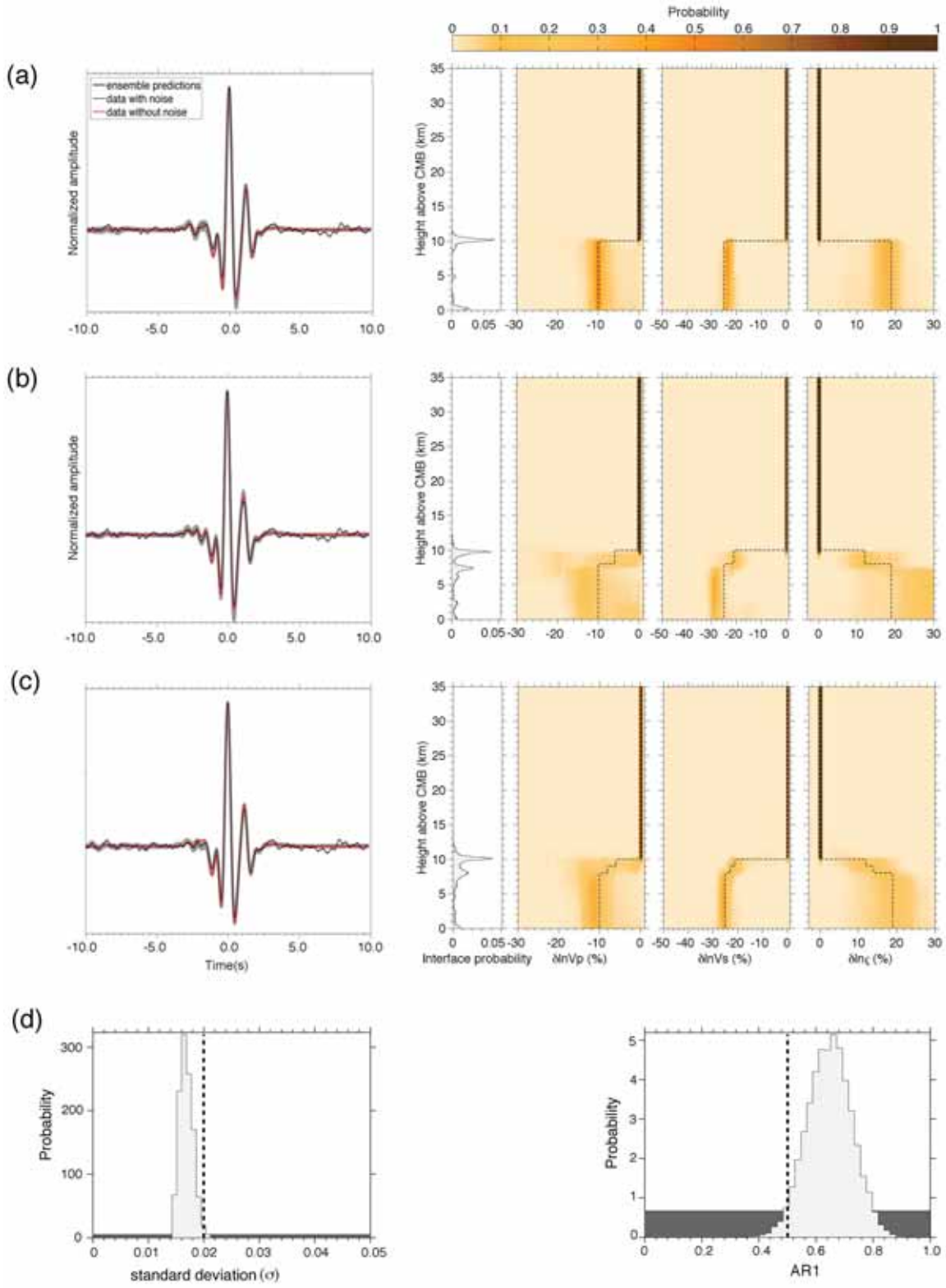

Figure 2. Sensitivity tests for increased complexity at the top of the ULVZ. Left-hand column: the simulated ScP-waveforms without noise (red), with noise (black) and ensemble of model predictions (grey lines). Right-hand column: Inversion results in terms of profile marginal probability densities for interface probability and perturbations of *P*-wave velocity, *S*-wave velocity, and density in the case of (a) one layer, (b) two layers and (c) three layers. True values (dashed lines) are also shown and presented in the text. Prior bounds for ULVZ parameters correspond to the plot widths while those for transition layer parameters are set to ± 1.0 per cent with respect to ak135. (d) Marginals of standard deviation for correlated errors (left), and AR1 parameter (right), prior (shaded) and true values (dashed). Prior bounds are from 0.0 to 0.2 and -0.5 to 0.99 for standard deviation and AR1, and normalized to unit area.

estimates, the inversion over-estimates the *S*-wave velocity, *P*-wave velocity and density perturbations of the bottom layer. In contrast, the inversion underestimates the bottom layer height because of the trade-off between *S*-wave velocity and layer thickness. The uncertainties in the bottom layers are from ∼−16 to 0 per cent, ∼−31 to −24 per cent and ∼20 to 30 per cent for *P*-wave velocity, *S*-wave velocity and density, respectively. Similarly, the *P*-wave velocity, *S*-wave velocity and density uncertainties in the top layer are from ∼−25 to 0 per cent, ∼−28 to −16 per cent and ∼6 to 22 per cent, respectively. This shows that the uncertainties for ULVZ parameters as well as interface probability increase substantially in comparison to that in the inversion of the first simulation. Similarly, the uncertainty for the top layer is higher than that for the bottom layer. The increase in uncertainty is likely due to the weak impedance contrast between the bottom layer and the layer between 8 and 10 km.

Next, we consider an additional interface to simulate an even smoother change in all elastic properties. The ScP waveform is simulated for a ULVZ in which the *P*-wave velocity perturbations are −6, −8 and −10 per cent, *S*-wave velocity perturbations are −21, −23 and −25 per cent, and density perturbations are 12, 14 and 19 per cent (from top to bottom). Fig. 2(c) shows the simulated data with and without noise. The trans-D approach developed here fits the data predominantly with a parsimonious 2-interface model (Fig. 2c) but also probabilistically includes more interfaces that appear to account for some of the smooth structure. The interfaces at 8 and 10 km are well resolved, with a lower probability for an interface at 8 km. A region of significant interface probability between 8- and 10-km heights marks the complex zone with smooth variation in velocity and density. The smooth variation is recovered well for both *S* velocity and density. The *P*-wave velocity is less well resolved which means that varying *P*-wave velocity structure does not have as much effect on the incident *S* wave as varying *S*-wave velocity and density.

The marginals of the noise parameters appear to be estimated reasonably well (Fig. 2d). The standard deviation of the noise is slightly underestimated while the correlation coefficient is overestimated. Other realizations of correlated and uncorrelated Gaussian noise were also examined (not shown here). These inversions generally show that parameter uncertainty increases with increases in correlation and standard deviation.

3.2.2 Increased complexity near the bottom of the ULVZ

This section presents inversions of simulated data that sample different ULVZ structures near the bottom of the ULVZ. The first simulation is for a single-layer ULVZ of 4-km height with 10 per cent decrease in *P*-wave velocity, 25 per cent decrease in *S*-wave velocity, and 19 per cent increase in density, the perturbation values used in our previous experiment. Simulated noise for AR1 correlation with the parameter values described previously is added to the simulated data. Fig. 3(a) shows the simulated ScP-waveforms with and without noise, the ensemble of model predictions, and inversion results. The inversion recovers all ULVZ parameters, although the uncertainty is large for *P*-wave velocity and density perturbations. The *P* velocity, *S* velocity, and density uncertainties are from ∼−14 to 0 per cent, ∼−30 to −23 per cent and ∼12 to 24 per cent, respectively. Additionally, the inversion correctly identifies the discontinuity at 4 km height from the CMB.

Next, we consider increased model complexity by adding an intermediate interface at 2 km above the CMB. The ULVZ parameters for the bottom layer are the same as in the previous case while the *P*-wave velocity, *S*-wave velocity, and density perturbations in the top layer are set to −6, −21 and 12 per cent, respectively. Although visual inspection does not show a significant change in the simulated data, the inversion results (Fig. 3b) show noticeable changes for all model parameters in comparison to those of the first simulation (Fig. 3a). The inversion averages over the parameter values of the two layers for *S*-wave velocity and density. The *S*-wave velocity and density uncertainties are similar while the *P*-wave velocity uncertainty is lager in this inversion. The inversion cannot resolve the interface and associated parameters at 2 km height, likely because the impedance contrast of an interface at 2 km is too weak to produce a strong reflection from that layer to be significant with respect to the strong CMB reflection at this noise level. Additionally, any weak reflections are also masked by the coda from interfaces at larger heights. Lastly, some information about the structure is present in the data. While the interface probability is smeared out over depth, indicating that the information is not sufficient to fully resolve the structure. We also performed the inversion by adding an additional interface at 3 km that further smoothed the changes in velocity and density. The resulting waveform does not change significantly but parameter values appear to be averaged and uncertainties are increased, particularly for *P*-wave velocity and density (Fig. S1).

Our synthetic experiments reveal that the fine structure within the first 3 km from the CMB cannot be resolved by the ScP waveforms considered here. Such limitations in resolution are due to noise in the data and the weakness of the impedance contrast and are likely realistic for observed data as well. For instance, a physically stable ULVZ is generally expected to have an increase in density and a decrease in velocity as a function of depth, which intrinsically reduces the impedance contrast. Due to a weak impedance contrast at 2/3-km height, amplitudes of pre- and post-cursors, which carry information about the discontinuity, remain undetected. To demonstrate this argument, we perform an inversion for the case where the impedance contrast is strong at 3 km height above the CMB. The ScP waveform is simulated for a ULVZ with two interfaces at 10 and 3 km height from the CMB. In this case, the bottom layer has the same *P*- and *S*-wave velocities as in the first case but the density perturbation is set to 12 per cent with respect to ak135. The *P*- wave and *S*-wave velocities, and density at the top layer are set to −6, −21 and 19 per cent, respectively, which introduces a gradual decrease for *P*- wave velocity, *S*-wave velocity and density. The decrease in density instead of increasing it as a function of depth increases the impedance contrast. The inversion results are shown in Fig. 3(c). The waveform significantly changes in comparison to those in previous cases in that all the pre- and post-cursors are visible. The inversion recovers all ULVZ parameters reasonably well. Moreover, the true interfaces at 10 and 3 km are clearly recovered. The noise parameter values (standard deviation and autocorrelation coefficients) are also recovered well (Fig. 3d). Additional inversions were performed for simulated data that sample a single layer with various ULVZ heights. These inversions show that the ULVZ parameters can be recovered even for a 2 km thick layer at the bottom if uncorrelated noise is considered. However, the inversion cannot recover ULVZ parameters if the strongly correlated noise is added. Overall, these simulations suggest that the ULVZ structure near the CMB cannot be recovered well when the impedance contrast is weak and the reflections from the top of ULVZs are masked by the strong CMB arrival.

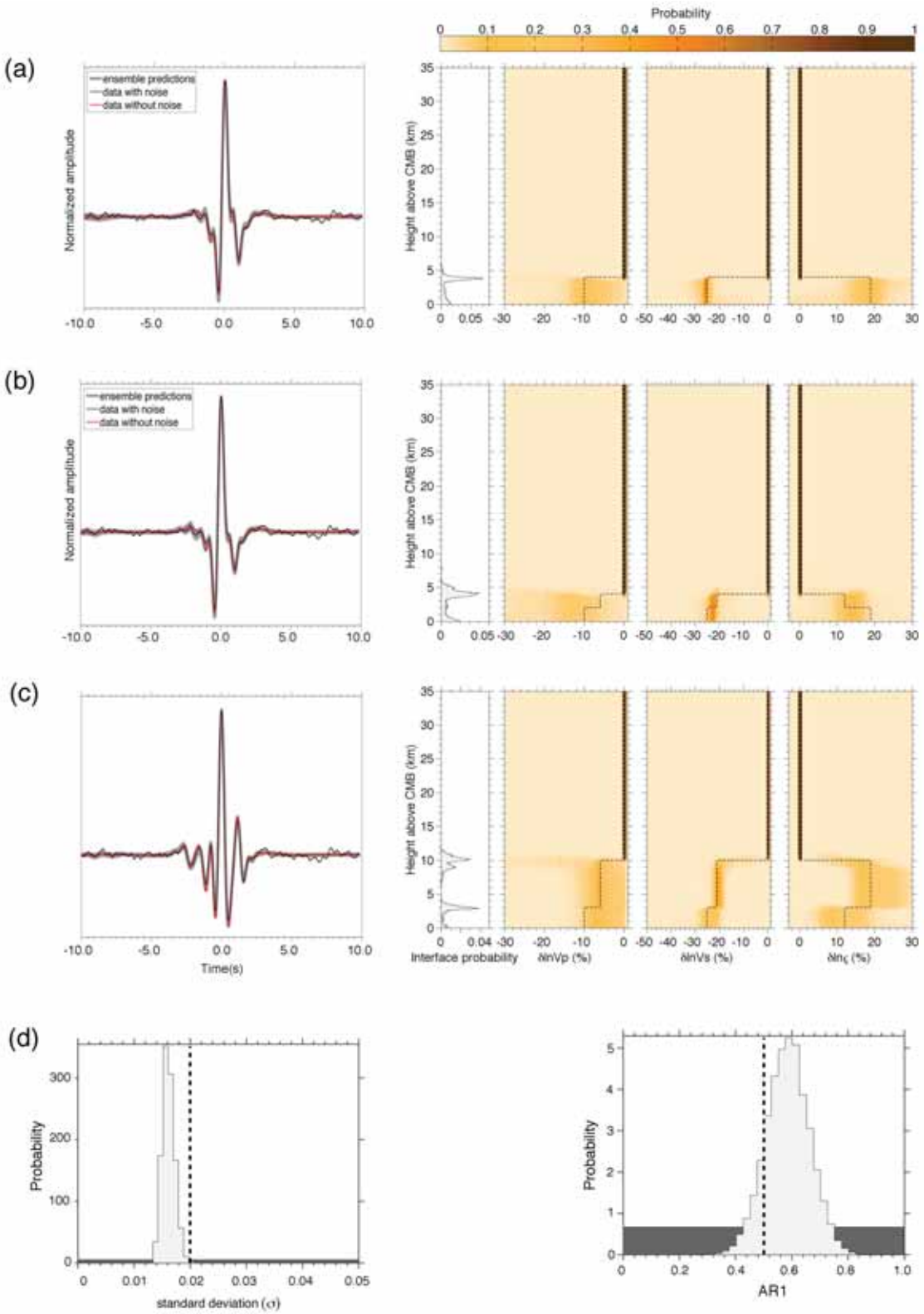

Figure 3. Sensitivity tests for increased complexity near the bottom of ULVZ with different impedance contrast. Left-hand column: the simulated ScP-waveforms without noise (red), with noise (black), and ensemble of model predictions (grey lines). Right-hand column: Profile marginals of interface probability and perturbation of *P*-wave velocity, *S*-wave velocity, and density in the case of (a) one layer, (b) two layers, and (c) two layers with strong impedance contrast. True values (dashed lines) are also shown. (d) Marginals of standard deviation for correlated errors (left), and AR1 parameter (right), prior (shaded) and true values (dashed).

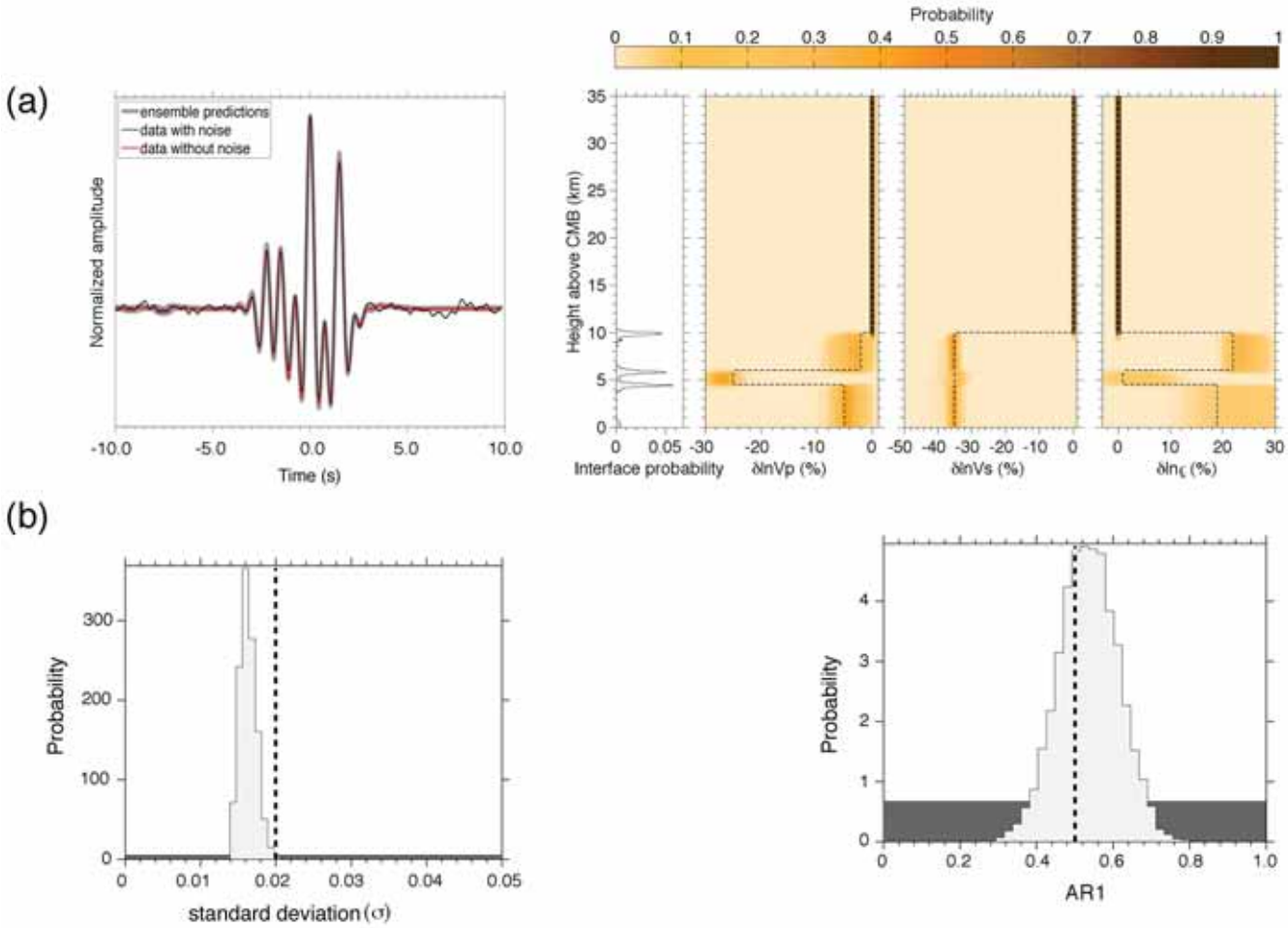

Figure 4. Resolution study for strong *P*-velocity and weak density structure sandwiched between weak *P*-velocity and strong density perturbations. (a) Left-hand column: the simulated ScP-waveforms without noise (red), with noise (black) and ensemble of model predictions (grey lines). Right-hand column: Profile marginals of interface probability and perturbation of *P*-wave velocity, *S*-wave velocity and density. (b) Marginals of standard deviation for correlated errors (left), and AR1 parameter (right), prior (shaded) and true values (dashed).

3.2.3 Simulation with a sandwiched layer

Motivated by the inversion results for the Philippine Sea ULVZ, we perform an additional sensitivity test for complex *P*-wave velocity and density structure and simple *S*-velocity structure. The ScP waveform is simulated for a three-layer ULVZ with interfaces at 10.0, 5.5 and 4.5 km above the CMB. The *P*-wave velocity perturbations are −2, −25 and −5 per cent, the *S*-wave velocity perturbations are −35, −35 and −35 per cent, and the density perturbations are 22, 1 and 19 per cent (top to bottom), resulting in a 'sandwich' layer. The inversion results (Fig. 4a) in terms of marginal profiles show that parameter values are well recovered. The recovery of noise parameters is shown in Fig. 4(b). This inversion demonstrates that a 1-km-thick structure in the middle of a 10-km-thick ULVZ can be resolved if the impedance contrast is strong.

The uncertainty analysis via trans-D Bayesian sampling provides clear results for resolution and an important result from the simulations is that parameter estimates appear more uncertain when the complexity of the ULVZ increases. Therefore, the ability to estimate ULVZ parameters decreases when complexity increases which may explain some of the controversies for regions with complex structure and emphasizes the importance of uncertainty analysis. Note that the detailed resolution studies carried out here are only possible when uncertainties are rigorously quantified. Estimating the posterior density allows us to precisely study how well parameters are resolved as a function of height from the CMB while accounting for (marginalizing over) the effects of all other relevant parameters. This is a significant advantage over other approaches that rely on forward modelling and subjectively choosing parameter combinations for sensitivity studies and/or holding some parameter values fixed while varying others.

4 RESULTS AND DISCUSSION

4.1 Results for Philippine Sea data

To study the CMB beneath the Philippine Sea, we consider the source location, station geometry, and ScP ray paths shown in Fig. 5(a). The same data were previously considered and are analysed here to rigorously compare trans-D inversion with the previous approach (Pachhai *et al.* 2014). The PcP and ScP waves are collected for a single event recorded on the Hi-net array, which consists of more than 600 short-period borehole stations (Okada *et al.* 2004).

A bandpass filter with corner frequencies of 0.5 and 1.5 Hz is applied for both PcP and ScP waveforms in a 60-s time window (centred on the main arrival) so that the central part of the signal is unaffected. Before stacking, waveforms are aligned on peak amplitudes of ScP and PcP waves separately. The stacked PcP

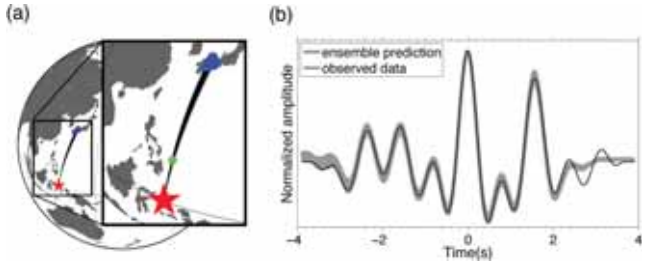

Figure 5. (a) Lowermost mantle beneath the Philippine Sea. The Indonesian earthquake location (star), surface projections of ScP ray paths (black lines) and Japanese Hi-Net Array stations (triangles) are shown. Reflection points at the CMB (green circles) are also shown. (b) Observed, stacked PcP-deconvolved ScP waves (black) and range of data predictions for the PPD (grey-shaded area).

waveform is then deconvolved from individual ScP waves to remove source and path effects. Cluster analysis is applied to form geographical clusters of similar waveforms. This yields two distinct clusters. The waveforms of the northeastern cluster are finally stacked to enhance the lowermost mantle features and reduce incoherent noise. This results in a waveform which will be considered as the observed waveform hereafter. A complete account of our data processing and cluster analysis can be found in Pachhai *et al.* (2014).

Our observed waveform (black line) and a range of predictions (grey shading) are shown in Fig. 5(b). Priors for the transition and ULVZ layers are set identical to our previous study (Pachhai *et al.* 2014) for comparison purposes. The likelihood is computed in an 8-s time window around the central peak of the ScP wave. Fig. 6(a) shows the rjMCMC sampling history and marginal probability of the number of interfaces. The large number of jumps between different numbers of interfaces indicates that the sampling works well. Figs 6(b) and (c) show the marginal probabilities of the error parameters (AR1 coefficient and σ). The AR1 coefficient indicates strongly correlated residual errors but also significant uncertainty in the value of the coefficient. Furthermore, the algorithm almost always includes the AR1 parameter in the error model, emphasizing that the residual errors are strongly correlated.

Profile marginal densities of the elastic parameter perturbations (Fig. 7a) show a complex ULVZ characterized by a thin layer (∼1.5 km) with strong *P*-wave velocity and weak density perturbations sitting between two layers of strong density perturbations. In the surrounding layers, the *P*-wave velocity perturbation is small and has a wide uncertainty, between ∼−15 and 1 per cent, while the density perturbation is weakly constrained with wide uncertainties between ∼5 and 30 per cent, nonetheless a positive perturbation of (at least) ∼5 per cent is required by the data. The *S*-wave velocity perturbations are unchanged for all layers and they are constrained well within prior bounds with a strong decrease in *S*-wave velocity ∼−45 to −30 per cent. The vertical extent of the ULVZ can reach up to 11 km from the CMB. The joint marginal distributions at discrete heights of 3 km and 5 km indicate strong parameter trade-offs (correlations, Fig. S2). In particular, strong correlations between *P*- and *S*-wave velocity as well as *S*-wave velocity and density perturbations are visible while the marginal for *P*-wave velocity and density shows no correlation.

A comparison of the trans-D results to our previous results (Pachhai *et al.* 2014) is also shown in Fig. 7. The previous study was based on model selection with the BIC and the optimal solution featured a ULVZ with two interfaces (Fig. 7b). It is important to note that the BIC cannot quantify relative model quality beyond identifying a single optimal model. As a result, it identified a single optimal solution and the ULVZ with three interfaces (Fig. 7c) was rejected. However, visual inspection of Figs 7(a) and (c) indicates that the trans-D results in this study include aspects of both solutions. This result emphasizes a significant limitations of using the BIC (or similar criteria that provide single optimal parametrizations) for model selection. Trans-D inversion generalizes model selection to simultaneously consider multiple reasonable models by quantifying the relative probability of each model (i.e. it provides a probability distribution for the considered models) and provides more general results that account for the uncertainty due to model specification. While much of the profiles agree to within the estimated uncertainties, the uncertainties are substantially larger (and more realistic) in the trans-D case. In particular, the uncertainties of interface probabilities increase substantially.

The main similarity in all results is a significant agreement in the *S*-wave velocity perturbation. The differences are exacerbated for *P* velocity and density perturbations. Our resolution test presented in Section 3.2.3 demonstrates that the inversion can, in principle, resolve a thin layer with a weak density perturbation sandwiched between two layers with strong density perturbations. We note that the sandwiched layer can be an artefact due to unaccounted effects

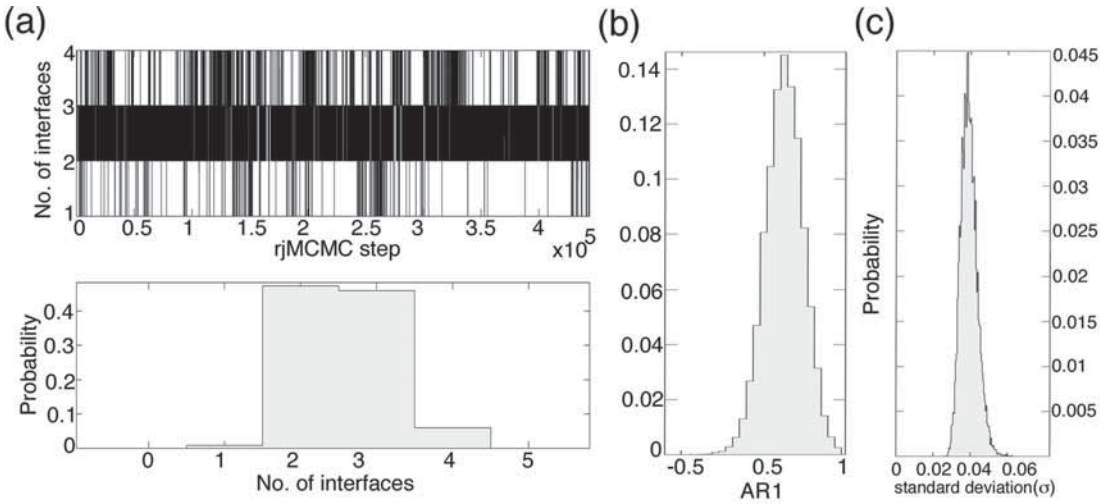

Figure 6. Inversion results for Philippine Sea data. (a) History of reversible jumps MCMC (top) and interface probability (bottom). (b) Mariginal densities of AR1 parameter and (c) standard deviation.

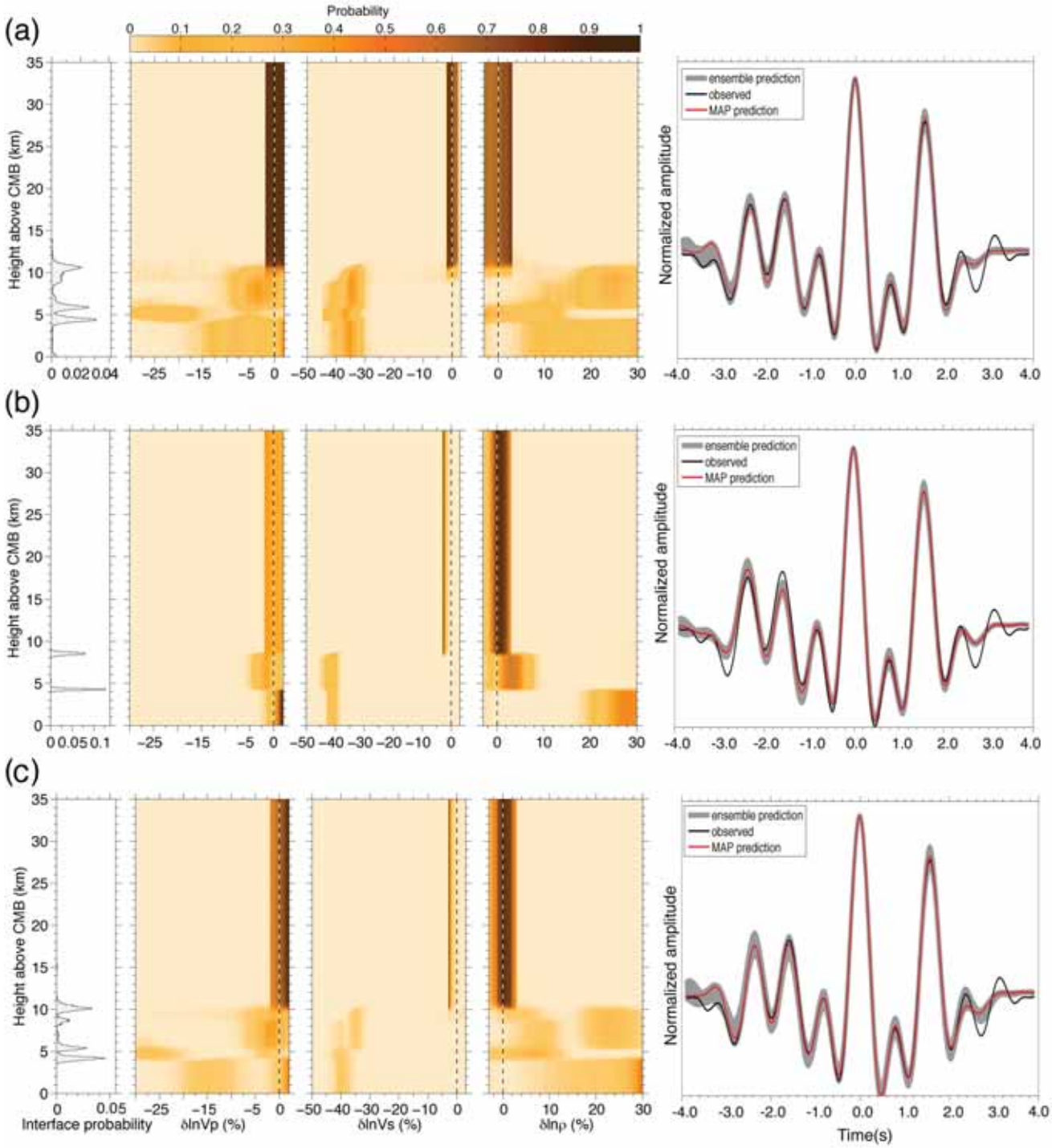

Figure 7. Comparison of Philippine Sea inversion results from this study to results from a previous study. Left-hand column: Profile marginal densities for interface probability and perturbation of *P*-wave velocity, *S*-wave velocity and density from (a) this study, (b) 2-layer model picked by BIC and (c) 3-layer model rejected by BIC in previous study are shown. Prior bounds for ULVZ parameters correspond to the plot widths while those for transition layer parameters are described in the text. Right-hand column: the observed ScP-waveforms without noise (red), with noise (black) and ensemble of model predictions (grey lines) are shown.

in the forward problem (e.g. 2-D/3-D nature of ULVZ, topography, anisotropy). However, if real, it is not straightforward to interpret and more multidisciplinary studies will be needed to further interpret this feature.

In summary, our inversion results for the Philippine Sea data support a ULVZ with a strong decrease in *S*-wave velocity and an increase in density. While the uncertainties of the density perturbation are large, the perturbation is likely $>+5$ per cent. The large uncertainties are due to body waves not being highly sensitive to density. It is important to note that the much smaller uncertainty estimates in the BIC study (Pachhai *et al.* 2014) may lead to interpreting structure that is not clearly supported by the data (Fig. 7).

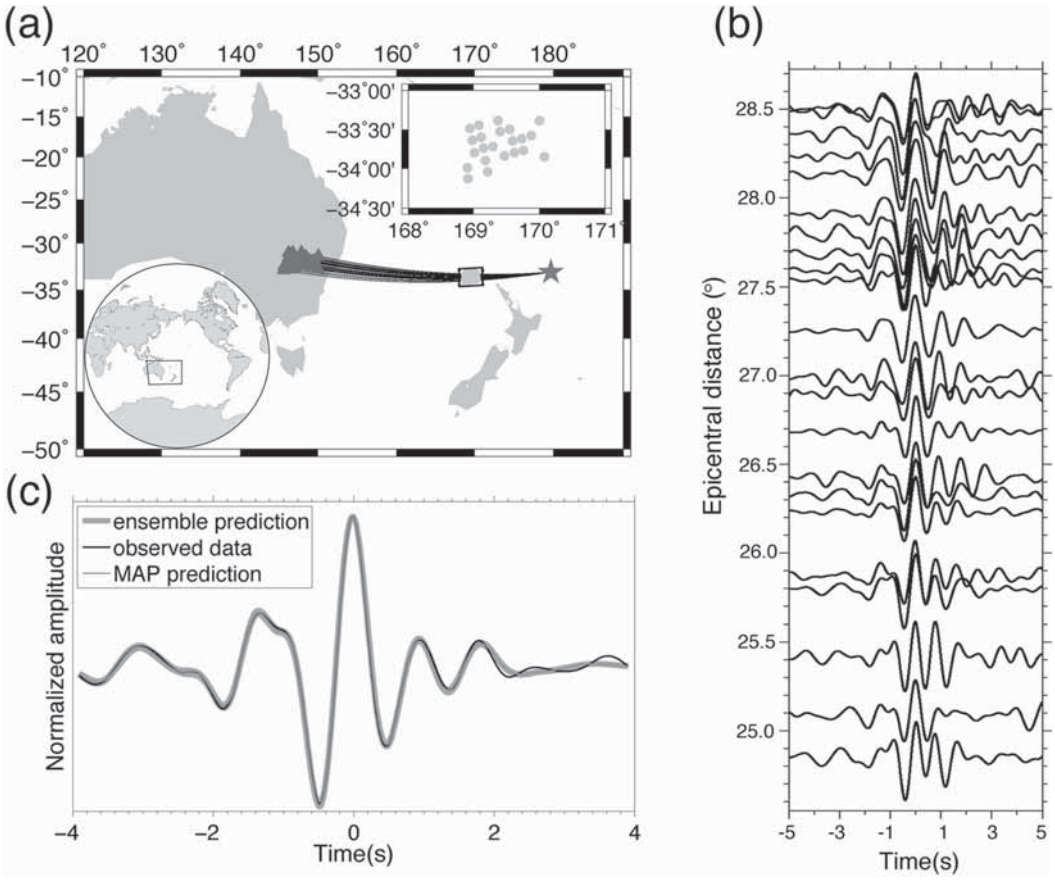

Figure 8. (a) Lowermost mantle region beneath the Tasman Sea. Earthquake (star) location near Vanautu Island in the southwest Pacific subduction zone, stations (triangle) from EAL2 sub-array in southeast Australia, ScP reflection points at the CMB, and ray paths (black lines) are shown. Details of reflection points are shown on the top-right corner. (b) Deconvolved-ScP waves used in this study are plotted according the epicentral distance. (c) Details of stacked waves (black line) and ensemble of model predicted data (grey colour) are shown.

The *P*-wave velocity perturbation is weak and more uncertain than *S*-wave velocity. Since the density perturbation is likely high and *P*-wave velocity perturbation is weak, the observed ULVZ structure is unlikely due to partial melting. Conversely, the iron enrichment could explain the decrease in velocity and increase in density (Wicks *et al.* 2010).

4.2 Inversion results for Tasman Sea data

The second data set considers waveforms sampling the lowermost mantle beneath the Tasman Sea (Fig. 8). The ScP waveforms are recorded by the WOMBAT transportable seismic array (EAL2 sub-array) in Australia (Rawlinson *et al.* 2008). The majority of the WOMBAT array stations are equipped with vertical, short-period seismometers at ∼50-km spacing. In contrast to the Hi-net array in Japan, the EAL2 subarray consists of significantly fewer stations (35–40). The sensors are enclosed in PVC cylinders and dug into the ground to the depth of about 40–80 cm. From these recordings, all PcP waveforms exhibiting complex features are discarded to comply with our requirement that PcP waves sample the CMB outside the ULVZ while ScP waves sample the ULVZ. Therefore, the number of recordings available from the WOMBAT array is limited.

To exploit the coherency of the arriving pre- and post-cursors, adaptive stacking (Rawlinson & Kennett 2004) is applied, which iteratively minimizes the misfit between the stacked waveform and individual waveforms to obtain optimal alignment. The individually aligned and deconvolved waveforms are shown in Fig. 8(b). These data show little variation in post-cursory amplitudes, but precursors are consistent over all the deconvolved waveforms. To examine whether these precursors are related to ULVZ or other unrelated phases, we sort the observed waveforms according to their azimuth, backazimuth and epicentral distance, using the maximum amplitude of the ScP waves to align the waveforms. We do not see evidence of the precursory phase move-outs with respect to the main phase (Figs 8b and S3). This indicates that waveform complexities (i.e. pre- and post-cursors) are linked to ScP waves. The final stacked waveform is also shown (Fig. 8c). The final ScP waveform used in the inversion is compared with an ensemble of waveform predictions based on most likely models (Fig. 8c). Joint marginal distributions for ULVZ parameters at different heights (1 and 3 km) are shown in Fig. S4 and indicate similar correlations that we observe in the case of the Philippine Sea data.

The inversion results in terms of marginal distributions of model parameter perturbations are shown in Fig. 9. A strong *S*-wave velocity perturbation, which gradually increases towards the CMB, dominates these profiles. The *S*-wave velocity is relatively well constrained with narrow uncertainties. The *P*-wave velocity and density are weakly constrained with significantly large uncertainties. However, density clearly exhibits a positive perturbation and *P*-wave velocity a negative perturbation. The extreme values in the bottom-most part (below 3 km) appear physically implausible, although our inversion is able to detect such a thin layer as shown in our sensitivity analysis in Section 3.2 Figs 2c and 3c. The

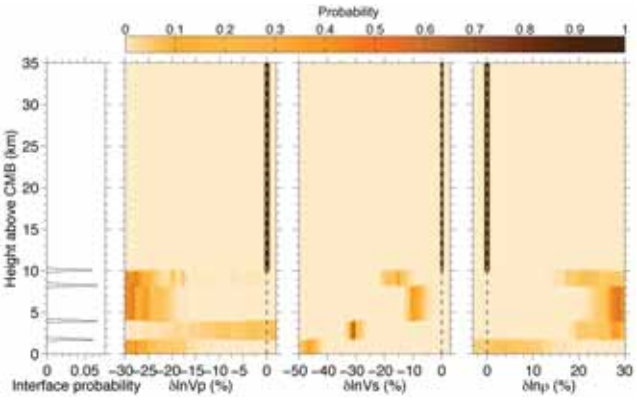

Figure 9. Profile marginal densities for interface probability and perturbation of *P*-wave velocity, *S*-wave velocity, and density for the data sampling the lowermost mantle beneath the Tasman Sea. Prior bounds for ULVZ parameters correspond to the plot widths while those for transition layer parameters are set to ±1.0 per cent with respect to ak135.

low-density perturbation does not match the strongly negative *S*-wave velocity. It can be argued that the resulting complex ULVZ parameter values are due to the variability of ScP waveforms caused by the lateral variability of ULVZ structure (since ULVZ structure can vary within a Fresnel zone). Such lateral variation can be identified by means of cluster analysis similar to that applied for the Philippine Sea data (Pachhai *et al.* 2014). However, the relatively small number of recordings available from a subarray of WOMBAT per event precludes such analysis. As an alternative approach, we remove the noisiest 10 per cent of the waveforms (characterized by ringing) from the dataset featured in Fig. 8(b). The waveform stacks before and after removing those waveforms are compared in Fig. S5. These waveforms closely match each other except for minor differences in post-cursor amplitudes. We also note that inversion results for these waveforms are not significantly different from the original results (Fig. S6).

It also can be suspected that some of the ringing precursors in the deconvolved ScP waveforms are due to the deconvolution itself. However, we note that water-level deconvolution was applied and the regularization parameter is tuned in such a way that the deconvolution does not introduce any artificial features (a similar experiment was performed in Pachhai *et al.* 2014). Additionally, the deconvolution parameter is sampled in the inversion to remove any bias and let data estimate this parameter. Example waveforms before and after the deconvolution are shown in Fig. S7. Note that no artificial features exist in the deconvolved waveforms, but precursors are more coherent after the deconvolution.

The results for the Tasman Sea data point to an even more complex ULVZ with three internal interfaces in comparison with two interfaces for the Philippines Sea. The profiles are dominated by a well-constrained, increased negative *S*-wave velocity perturbation as a function of depth. Density and *P*-wave velocity have higher uncertainties, but density likely has a strong positive perturbation (with lower uncertainty in comparison to that in the Philippine Sea data). Moreover, two different features are visible in this region, particularly for *P*-wave velocity and density. The *P*-wave velocity remains strong and is at similar values for the layers between 4 and 10 km with wider uncertainties. The *P*-wave velocity in a layer between 2 and 4 km has weak perturbation with even wider uncertainties (from ∼−20 to 0 per cent). Similarly, the density perturbation is strong and exhibits similar values for the layers between 2- and 10-km height with uncertainties from ∼20 to 30 per cent. The density perturbation becomes close to zero and *P*-wave perturbation is strong (∼−28 per cent) in the lowermost layer.

The upper layers can be explained by the partial melting of the iron-rich material originating in the core. However, the lowermost layer has a strong decrease in *S*- and *P*-wave velocities and a weak increase in density (<∼14 per cent). For a gravitationally stable ULVZ at the bottom of the mantle, we do not expect to see a density perturbation weaker in comparison to that in the layers above it. Therefore, we speculate that this reflects imperfections in our forward model. In particular, our model fixes the CMB position at the ak135 value and no topography is accounted for. A recent study shows a maximum CMB topography height of up to ±2 km with an uncertainty of 0.5 km (Tanaka 2010). A more realistic CMB is most likely characterized by lateral heterogeneities on both sides of the boundary. For example, it has been proposed that the sedimentation of lighter elements in the outer core might occur through chemical reactions at the CMB (Buffett *et al.* 2000). These layers are not accounted for in our inversion and it is possible that this additional structure is mapped to the marginal distributions as a lowermost layer with non-familiar properties. The bottom layer could also be explained by the reaction of basaltic melt with the volatile gas coming from the core if the physical origin of the ULVZ is due to the partial melting of mid-oceanic ridge basalt subducted through the slab (e.g. Andrault *et al.* 2014).

Apart from the multiple-layer 1-D structure, the multiple post-cursors in Fig. 8(b) may be a result of multipathing effects caused by the volume of the ULVZ that is not represented well by a 1-D model. However, while the computational cost required to account for 3-D structure precludes the use of 3-D parametrizations in Bayesian analysis, our inversion approach accounts for path effects except those due to edge effects. To demonstrate the performance of our inversion for the case of an inaccurate background earth model, we perturbed the *S*-wave velocity in the lowermost mantle region (∼300 km from the top of the CMB) of the ak135 background model by −3.5 per cent. This perturbation is consistent with most results from *S*-wave velocity tomography for the lowermost mantle. Then, a single-layer ULVZ with −10 per cent change in *P* velocity, −25 per cent change in *S* velocity, and 19 per cent change in density is added to the perturbed ak135 model. The ScP waveform is computed for this ULVZ model whereas the PcP waveform is computed for an unperturbed (ak135) background model. We then deconvolve the PcP waveform from the ScP waveform in accordance with our assumption that PcP and ScP waves travel different paths in the lowermost mantle region and that the PcP wave does not sample the ULVZ. Gaussian random noise with standard deviation $\sigma = 0.02$ is added to the deconvolved ScP waveform to complete the simulated data. We carried out the inversion with the unperturbed ak135 model as the background model (the inversion results with and without including the AR1 parameter are shown in Fig. S9). The inversion recovers all parameter values well in both cases. However, parameter uncertainties for *P*-wave velocity and density are higher in the case where we include the AR1 coefficient in the inversion.

5 CONCLUSIONS

We developed a trans-D hierarchical Bayesian inversion to rigorously quantify ULVZ parameters and their uncertainties using ScP waveforms. The inversion treats the number of layers and the vertical extent of the trans-D ULVZ model as unknowns. The inversion also considers the noise parameters (i.e. autoregressive coefficients of order 1 and standard deviation) as unknown to address correlated data errors. This approach quantifies the unknown model

parametrization resulting in meaningful quantification of parameter values and their uncertainties based on the data information. Reversible jump Markov chain Monte Carlo sampling with parallel tempering was applied to improve the sampling efficiency.

The trans-D inversion was first applied to various simulated data that sample the structure of increasing complexity in both velocity and density. The inversion of simulated ScP waveforms with correlated data errors recovered all ULVZ and noise parameters well when the impedance contrast is high and level of noise is reasonable. Structures near the top of ULVZs were better resolved than structures near the bottom at the same level of noise. This is due to the weak impedance contrast, which reduces the amplitude of the first arrivals resulting from the top of the ULVZ. Additionally, the reflections from the top are not masked by any previous arrivals, whereas the reflections from the bottom come with the coda of the layers above. It is also difficult to use the information from possible reverberations because the CMB reflection is strong and can mask such arrivals. However, the inversion reasonably quantifies such structure by averaging over layers at increased parameters uncertainty. The inversion can recover all parameters if less and uncorrelated noise is considered. In comparison, the inversion recovers *S*-wave velocity perturbations generally well with narrow uncertainty because of the high sensitivity of ScP waveforms to *S*-wave velocity contrasts.

Recorded ScP waveforms that sample the CMB beneath the Philippine and Tasman Seas are also considered. The inversion results for the Philippine Sea data exhibit a strong decrease in *S*-wave velocity and no significant decrease in *P*-wave velocity while the density perturbations are positive with large uncertainty. The trans-D results are comparable with those of a previous study that considers an optimal but fixed parametrization (BIC based) in that the *S*-wave velocity perturbation is strong and the *P*-wave perturbation is weak. However, uncertainties of ULVZ parameters are significantly higher in the case of the trans-D inversion in comparison to that in the BIC inversion, exposing significant limitations in the BIC approach. The inversion results for the Tasman Sea data show a well-constrained *S*-wave velocity with a gradual decrease as a function of depth. Results further suggest two distinct classes of structures. The upper layers can be due to the partial melting of iron-rich material in the lowermost mantle. The lowermost layer may be an artefact due to imperfections of our forward model. For example, the sedimentation of lighter elements in the outer core is not accounted for and it is possible that this is mapped into the marginal distributions of model parameters.

With almost every new observation, it is clear that the CMB is not a featureless boundary. The two ULVZs studied here both exhibit different structure, but are similar in complexity. Our inversions point to large uncertainties in *P*-wave velocity and density perturbations. Limited *P*-wave velocity sensitivity is likely a general problem for ScP data and may be difficult to overcome. Resolving density is even more challenging since seismic waves are only weakly sensitive to density. Due to the high uncertainty in *P*-wave velocity and density perturbations in both cases, it is difficult to fully distinguish the partial melt origin from iron enrichment. Yet, the technique developed here presents a considerable step forward in deciphering ULVZ morphology, by equipping us with more objective ways to quantify uncertainty and non-uniqueness. Although our forward model assumptions are still simple, with more computational power, further advances in efficient, parsimonious 2-D and 3-D parametrizations, and advanced sampling techniques, it should eventually become possible to account for lateral variability in elastic structure and shape of ULVZs.

ACKNOWLEDGEMENTS

We would like to thank the editor D. Shim for handling this manuscript, and M. Thorne and an anonymous reviewer for providing valuable comments on the manuscript. Computations were performed on the Terrawulf II and III cluster, a computational facility supported through the AuScope Australian Geophysical Observing System (AGOS). AuScope is funded under the National Collaborative Research Infrastructure Strategy (NCRIS) and the Education Investment Fund (EIF3), both Australian Commonwealth Government Programs.

REFERENCES

Agostinetti, P.N. & Malinverno, A., 2010. Receiver function inversion by trans-dimensional Monte carlo sampling, *Geophys. J. Int.,* **181,** 858–872.

Andrault, D., Pesce, G., Bouhifd, M.A., Casanova, N.B., Henot, J.-M. & Mezourar, M., 2014. Melting of subducted basalt at the core-mantle boundary, *Science,* **344**(6186), 892–895.

Berryman, J.G., 2000. Seismic velocity decrement ratios for regions of partial melt in the lower mantle, *Geophys. Res. Lett.,* **27,** 421–424.

Bodin, T. & Sambridge, M., 2009. Seismic tomography with the reversible jump algorithm, *Geophys. J. Int.,* **178,** 1411–1436.

Bréger, L., Tkalčić, H. & Romanowicz, B., 2000. The effect of D″ on PKP (AB-DF) travel time residuals and possible implications for inner core structure, *Earth planet. Sci. Lett.,* **175,** 133–143.

Brown, S.P., Thorne, M.S., Miyagi, L. & Rost, S., 2015. A compositional origin to ultralow-velocity zones, *Geophys. Res. Lett.,* **42,** 1039–1045.

Brüstle, W. & Müller, G., 1983. Moment and duration of shallow earthquakes from Love-wave modelling for regional distances, *Phys. Earth planet. Inter.,* **32,** 312–324.

Buffett, B.A., Garnero, E.J. & Jeanloz, R., 2000. Sediments at the top of Earth's core, *Science,* **290**(5495), 1338–1342.

Chapman, C.H. & Orcutt, J.A., 1985. The computation of body wave seismograms in laterally homogeneous media, *Rev. Geophys.,* **23**(2), 105–163.

Denison, D.G.T., Holmes, C.C., Mallick, B.K. & Smith, A.F.M, 2002. *Bayesian Methods for Nonlinear Classification and Regression,* Wiley, pp. 177–207.

Dettmer, J. & Dosso, S.E., 2012. Trans-dimensional matched-field geoacoustic inversion with hierarchical error models and interacting Markov chains, *J. acoust. Soc. Am.,* **132**(4), 2239–2250.

Dettmer, J., Dosso, S.E. & Holland, C.W., 2010. Trans-dimensional geoacoustic inversion, *J. acoust. Soc. Am.,* **128**(6), 3393–3405.

Dettmer, J., Dosso, S.E. & Holland, C.W., 2009. Model selection and Bayesian inference for high-resolution seabed reflection inversion. *J. acoust. Soc. Am.,* **125**(2), 706–715.

Dettmer, J., Molnar, S., Steininger, G., Dosso, S.E. & Cassidy, J.F., 2012. Trans-dimensional inversion of micrometer array dispersion data with hierarchical autoregressive error models, *Geophys. J. Int.,* **188,** 719–734.

Dettmer, J., Holland, C.W. & Dosso, S.E., 2013. Transdimensional uncertainty estimation for dispersive seabed sediments, *Geophys,* **78,** WB63–WB76.

Dobson, D.P. & Brodholt, J.P., 2005. Subducted banded iron formations as a source of ultralow-velocity zones at the core-mantle boundary, *Nature,* **434,** 371–374.

Doornbos, D.J., 1974. Seismic wave scattering near caustics: observation of PKKP precursors, *Nature,* **247,** 352–353.

Dosso, S.E., Dettmer, J., Steininger, G. & Holland, C.W., 2014. Efficient trans-dimensional Bayesian inversion for geoacoustic profile estimation, *Inverse Problems,* **30,** doi:10.1088/0266-5611/30/11/114018.

Garnero, E.J. & Helmberger, D.V., 1995. A very slow basal layer underlying large-scale low velocity anomalies in the lower mantle beneath the Pacific: evidence from core phases, *Phys. Earth planet. Inter.,* **91,** 161–176.

Garnero, E.J. & Helmberger, D.V., 1996. Seismic detection of a thin laterally varying boundary layer at the base of the mantle beneath the central-Pacific, *Geophys. Res. Lett.,* **23**(9), 977–980.

Garnero, E.J. & Helmberger, D.V., 1998. Further structural constraints and uncertainties of a thin laterally varying ultralow-velocity layer at the base of the mantle, *J. geophys. Res.,* **103**(B6), 12 495–12 509.

Garnero, E.J., Revenaugh, J., Williams, Q., Lay, T. & Kellogg, L.H., 1998. Ultralow velocity zone at the core-mantle boundary, in *The Core-Mantle Boundary Region,* eds Gurnis, M., Wysession, M.E., Knittle, E. & Buffett, B.A., Am. Geophys. Un., doi:10.1029/GD028p0319.

Garnero, E.J., Maupin, V., Lay, T. & Fouch, M.J., 2004. Variable azimuthal anisotropy in Earth's lowermost mantle, *Science,* **306,** 259–261.

Geyer, C.J., 1991. Markov chain Monte Carlo maximum likelihood, in *Computing Science and Statistics: Proceedings of the 23rd Symposium on the Interface,* Interface Foundation, Fairfax Station, VA, pp. 156–163.

Geyer, C.J. & Møller, J., 1994. Simulation procedures and likelihood inference for spatial point processes, *Scand. J. Stat.,* **21,** 359–373.

Green, P.J., 1995. Reversible jump Markov chain Monte Carlo computation and Bayesian model determination, *Biometrika,* **82,** 711–312.

Green, P.J., 2003. Trans-dimensional Markov chain Monte Carlo, in *Highly Structured Stochastic Systems,* Oxford Statistical Science Series, pp. 179–198, eds Green, P.J., Hjort, N.L. & Richardson, S., Oxford Univ. Press, Oxford.

Haddon, R.A.W. & Cleary, J.R., 1974. Evidence for scattering of seismic PKP waves near the mantle core boundary, *Phys. Earth planet. Inter.,* **8**(3), 211–234.

Helmberger, D., Ni, S., Wen, L. & Ritsema, J., 2000. Seismic evidence for ultralow-velocity zones beneath Africa and eastern Atlantic, *J. geophys. Res.,* **105,** 23 865–23 878.

Helmberger, D.V., Wen, L. & Ding, X., 1998. Seismic evidence that the source of the Iceland hotspot lies at the core-mantle boundary, *Nature,* **396,** 251–255.

Hutko, A.R., Lay, T. & Revenaugh, J., 2009. Localized double-array stacking analysis of PcP: D″ and ULVZ structure beneath the Cocos plate, Mexico, central Pacific, and north Pacific, *Phys. Earth planet. Inter.,* **173,** 60–74.

Idehara, K., 2011. Structural heterogeneity of an ultra-low velocity zone beneath the Philipine Islands: implications for core-mantle chemical interactions induced by massive partial melting at the bottom of the mantle, *Phys. Earth planet. Inter.,* **184,** 80–90.

Idehara, K., Yamada, A. & Zhao, D., 2007. Seismological constraints on the ultralow velocity zones in the lowermost mantle from core-reflected waves, *Phys. Earth planet. Inter.,* **165,** 25–46.

Jensen, K.J., Thorne, M.S. & Rost, S., 2013. SPdKS analysis of ultralow-velocity zones beneath the western Pacific, *Geophys. Res. Lett.,* **40,** 1–5.

Kennett, B.L.N., Engdahl, E.R. & Buland, R., 1995. Constraints on seismic velocities in the Earth from traveltimes, *Geophys. J. Int.,* **122**(1), 108–124.

Knittle, E. & Jeanloz, R., 1991. Earth's core-mantle boundary results of experiments at high pressures and temperatures, *Science,* **251,** 1438–1443.

Labrosse, S., Hernlund, J. & Coltice, N., 2007. A crystallizing dense magma ocean at the base of the Earth's mantle, *Nature,* **450,** 866–869.

Lay, T. & Helmberger, D.V., 1983. A lower mantle *S*-wave triplication and the shear velocity structure of D″, *Geophys. J. R. astr. Soc.,* **75,** 799–837.

Lay, T., Williams, Q. & Garnero, E.J., 1998. The core-mantle boundary layer and deep Earth dynamics, *Nature,* **392,** 461–468.

MacKay, D.J.C., 2003. *Information Theory, Inference, and Learning Algorithms,* Cambridge Univ. Press.

Malinverno, A., 2002. Parsimonious Bayesian Markov chain Monte Carlo inversion in a nonlinear geophysical problem, *Geophys. J. Int.,* **151**(3), 675–688.

Manga, M. & Jeanloz, R., 1996. Implications of a metal-bearing chemical boundary layer in D″ for mantle dynamics, *Geophys. Res. Lett.,* **23,** 3091–3094.

Mao, W.L. *et al.*, 2006. Iron-rich post-perovskite and the origin of ultralow-velocity zones, *Science,* **312,** 564–565.

Masters, G., Johnson, S., Laske, G. & Bolton, B., 1996. A shear-velocity model of the mantle, *Phil. Trans. R. Soc. Lond.,* **354,** 1385–1411.

Minsley, B.J., 2011. A trans-dimensional Bayesian Markov chain Monte Carlo algorithm for model assessment using frequency-domain electromagnetic data, *Geophys. J. Int.,* **187**(1), 252–271.

Okada, Y., Kasahara, K., Hori, S., Obara, K., Sekiguchi, S., Fujiwara, H. & Yamamoto, A., 2004. Recent progress of seismic observation network in Japan –Hi-net, F-net, K-net and KiK-net, *Earth Planets Spaces,* **56,** xv–xxviii.

Otsuka, K. & Karato, S., 2012. Deep penetration of molten iron into the mantle caused by morphological instability, *Nature,* **492,** 243–247.

Pachhai, S., Tkalčić, H. & Dettmer, J., 2014. Bayesian inference for ultralow velocity zones in the Earth's lowermost mantle: complex ULVZ beneath the east of Philippines, *J. geophys. Res.: Solid Earth,* **119,** 8346–8365.

Rawlinson, N. & Kennett, B.L.N., 2004. Rapid Estimation of relative and absolute network by adaptive stacking, *Geophys. J. Int.,* **157,** 332–340.

Rawlinson, N., Tkalcic, H. & Kennett, B.L.N., 2008. New results from WOMBAT: an ongoing program of passive seismic array deployments in Australia, *EOS, Trans. Am. geophys. Un.,* **89**(53), Fall Mett. Suppl., Abstract S22A-03.

Revenaugh, J. & Meyer, R., 1997. Seismic evidence of partial melt within a possibly ubiquitous low-velocity at the base of the mantle, *Science,* **277**(5326), 670–673.

Ringwood, A.E, 1979. *Origin of the Earth and Moon,* Springer-Verlag, 295 p.

Ringwood, A.E. & Hibberson, W., 1991. Solubilities of Mantle oxides in molten iron at high pressures and temperatures: implications for the composition and formation of Earth's core, *Earth planet. Sci. Lett.,* **102,** 235–251.

Rondenay, S., Cormier, V.F. & Van Ark, E.M., 2010. SKS and SPdKS sensitivity to two-dimensional ultralow-velocity zones, *J. geophys. Res.,* **115,** B04311, doi:10.1029/2009JB006733.

Rondenay, S. & Fischer, K.M., 2003. Constraints on localized core-mantle boundary structure from multichannel, broadband SKS coda analysis, *J. geophys. Res.,* **108,** 2537, doi:10.1029/2003JB002518,B11.

Rost, S. & Earle, P.S., 2010. Identifying regions of strong scattering at the core-mantle boundary from analysis of PKKP precursor energy, *Earth planet. Sci. Lett.,* **297,** 616–626.

Rost, S. & Revenaugh, J., 2003. Small-scale ultralow-velocity zone structure imaged by ScP, *J. geophys. Res.,* **108**(B1), 2056, doi:10.1029/2001JB001627.

Rost, S. & Thomas, C., 2002. Array seismology: methods and applications, *Rev. Geophys.,* **40**(3), 1008, doi:10.1029/2000RG000100.

Rost, R. & Thomas, C., 2009. Improving seismic resolution through array processing techniques, *Surv. Geophys.,* **30,** 271–299.

Rost, S., Garnero, E.J. & Stefan, W., 2010a. Thin and intermittent ultralow-velocity zones, *J. geophys. Res.,* **115,** B06312, doi:10.1029/2009JB006981.

Rost, S., Garnero, E.J., Thorne, M. & Hutko, A., 2010b. On the absence of an ultra-low velocity zone in the North Pacific, *J. geophys. Res.,* **115,** B04312, doi:10.1029/2009JB006420.

Rost, S., Garnero, E.J. & Williams, Q., 2006. Fine-scale ultralow-velocity zone structure from high-frequency seismic array data, *J. geophys. Res.,* **111,** B09310, doi:10.1029/2005JB004088.

Rost, S., Garnero, E.J., Williams, Q. & Manga, M., 2005. Seismological constraints on a possible plume root at the core-mantle boundary, *Nature,* **435,** 666–669.

Sambridge, M. & Moseguard, K., 2002. Monte Carlo methods in geophysical inverse problems, *Rev. Geophys.,* **40**(3), 1009, doi:10.1029/2000RG00089.

Sambridge, M., Gallagher, K., Jackson, A. & Rickwood, P., 2006. Trans-dimensional inverse problems, model comparison and the evidence, *Geophy. J. Int.,* **167,** 528–542.

Schwarz, G., 1978. Estimating the dimension of a model, *Ann. Stat.,* **6,** 461–464.

Soldati, G., Boschi, L. & Forte, A.M., 2012. Tomography of core–mantle boundary and lowermost mantle coupled by geodynamics, *Geophys. J. Int.,* **189,** 730–746.

Steininger, G., Holland, C.W., Dosso, S.E. & Dettmer, J., 2013. Seabed roughness parameters from joint backscatter and reflection inversion at the Malta Plateau, *J. acoust. Soc. Am.,* **134**(3), 1833–1842.

Tanaka, S., 2010. Constraints on the core-mantle boundary topography from *P4KP-PcP* differential travel times, *J. geophys. Res.,* **115,** B04310, doi:10.1029/2009JB006563.

Tarantola, A., 2005. *Inverse Problem Theory and Methods for Model Parameter Estimation,* SIAM.

Thomas, C., Kendall, J-M. & Lowman, J., 2004. Lower-mantle seismic discontinuities and the thermal morphology of subducted slabs, *Earth planet. Sci. Lett.,* **225,** 105–113.

Thorne, M.S. & Garnero, E.J., 2004. Inferences on ultralow-velocity zone structure from a global analysis of SPdKS waves, *J. geophys. Res.,* **109,** B08301, doi:10.1029/2004JB003010.

Thorne, M.S., Garnero, E.J., Jahnke, G., Igel, H. & McNamara, A.K., 2013. Mega ultra low velocity zones and mantle flow, *Earth planet. Sci. Lett.,* **364,** 59–67.

Thybo, H., Ross, A.R. & Egorkin, A.V., 2003. Explosion seismic reflections from the Earth's core, *Earth planet. Sci. Lett.,* **216,** 693–702.

Tkalčić, H. & Romanowicz, B., 2002. Short scale heterogeneity in the lowermost mantle: insights from PcP-P and ScS-S data, *Earth planet. Sci. Lett.,* **201**(1), 57–68.

Tkalčić, H., Romanowicz, B. & Houy, N., 2002. Constraints on D″ structure using PKP(AB-DF), PKP(BC-DF) and PcP-P traveltime data from broadband records, *Geophys. J. Int.,* **148,** 599–616.

Tkalčić, H., Young, M.K., Bodin, T., Nigo, S. & Sambridge, M., 2013. The shuffling rotation of the Earth's inner core revealed by earthquake doublets, *Nat. Geosci.,* **6,** 497–502.

To, A., Fukao, Y. & Tsuboi, S., 2011. Evidence for a thick and localized ultra low shear velocity zone at the base of the mantle beneath the central Pacific, *Phys. Earth planet. Inter.,* **184,** 119–133.

Wen, L. & Helmberger, D.V., 1998a. Ultra-low velocity zones near the core-mantle boundary from broadband PKP precursors, *Science,* **279**(1701), doi:10.1126/science.279.5357.1701.

Wen, L. & Helmberger, D.V., 1998b. A two-dimensional P-SV hybrid method and its application to modelling localized structures near the core-mantle boundary, *J. geophys. Res.,* **103**(B8), 17 901–17 918.

Wenk, H.-R., Cottaar, S., Tome, C.N., McNamara, A. & Romanowicz, B., 2011. Deformation in the lowermost mantle: from polycrystal plasticity to seismic anisotropy, *Earth. planet. Sci. Lett.,* **306,** 33–45.

Wicks, J.K., Jackson, J.M. & Sturhahn, W., 2010. Very low sound velocities in iron-rich (Mg,Fe)O: implications for the core-mantle boundary region, *Geophys. Res. Lett.,* **37,** doi:10.1029/2010GL043689.

Williams, Q. & Garnero, E.J., 1996. Seismic evidence for partial melt at the base of Earth's mantle, *Science,* **273,** 1528–1530.

Williams, Q., Revenaugh, J. & Garnero, E., 1998. A correlation between ultra-low basal velocities in the mantle and hot spots, *Science,* **281,** 546–549.

Wysession, M.E., 1996. Large-scale structure at the core-mantle boundary from diffracted waves, *Nature,* **382,** 244–248.

Wysession, M.E., Langenhorst, A., Fouch, M.J., Fischer, K.M., Al-Equabi, G.I., Shore, P.J. & Clarke, T.J., 1999. Lateral variations in compressional/shear velocities at the base of the mantle, *Science,* **248**(5411), 120–125.

Young, C. & Lay, T., 1987. The core-mantle boundary, *Ann. Rev. Earth planet. Sci.,* **15,** 25–46.

Young, M.K., Tkalčić, H., Bodin, T. & Sambridge, M., 2013. Global P-wave tomography of Earth's lowermost mantle from partition modelling, *J. geophys. Res.,* **118**(10), 5467–5486.

Zhang, L. *et al.*, 2014. Disproportionation of (Mg, Fe) SiO_3 perovskite in Earth's deep lower mantle, *Science,* **344,** 877–882.

SUPPORTING INFORMATION

Additional Supporting Information may be found in the online version of this paper:

Figure S1. Sensitivity test for complex ULVZ with three thin layers at the top of the CMB. (a) Simulated ScP-waveforms without noise (red), with noise (black) and the ensemble of model predictions (grey lines). (b) Profile marginals for interface probability and perturbations of *P*-wave velocity, *S*-wave velocity, and density. True values (dashed lines) are also shown and presented in the text. Prior bounds for ULVZ parameters correspond to the plot widths while those for transition layer parameters are set to ± 1.0 per cent with respect to ak135. (c) Marginals of the standard deviation for correlated errors (left), and the AR1 parameter (right), prior (shaded), and true values (dashed). Prior bounds are from 0.0 to 0.2 and -0.5 to 0.99 for standard deviation and AR1, and normalized to unit area.

Figure S2. Joint marginals of different parameters in the case of Philippine Sea data. (a) Profile marginals for interface probability and perturbations of *P*-wave velocity, *S*-wave velocity and density. Background 1-D parameter values (vertical dashed lines) and interface heights at which joint marginals are computed (horizontal dashed lines) are also shown. Joint marginals for various parameters at (b) 5 km and (c) 3 km heights are shown. Probability for joint marginals is normalized to unity.

Figure S3. Deconvolved ScP-waveforms sorted based on the azimuth and back-azimuth.

Figure S4. Joint marginals of various parameter pairs for the Tasman Sea data. (a) Profile marginals for interface probability and perturbations of *P*-wave velocity, *S*-wave velocity and density. Background 1-D parameter values (vertical dashed lines) and interface heights at which joint marginals are computed (horizontal dashed lines) are also shown. Joint marginals of various parameters at (b) 3 km and (c) 1 km heights are shown. Probability is normalized to unity.

Figure S5. Stacked waveforms before and after removing ringing waveforms for Tasman Sea data from Fig. 8(b).

Figure S6. Profile marginals for interface probability and perturbations of *P*-wave velocity, *S*-wave velocity and density obtained from the inversion of stacked waveform after removing ringing waveforms from the Tasman Sea data.

Figure S7. Comparison of ScP waveforms before and after the deconvolution by PcP for the Tasman Sea data. The waveforms before and after deconvolution do not differ significantly, which indicates that the complexity in the waveforms is not due to deconvolution.

Figure S8. (a) Simulated ScP-waveforms without noise (red), with uncorrelated noise (black) and ensemble of model predictions (grey lines). The ScP waveform is prepared assuming perturbed ak135 model as background model. A detailed description can be found in the text. (b) Profile marginals for interface probability and perturbations of *P*-wave velocity, *S*-wave velocity and density. True values (dashed lines) and uncertainty limits (green dashed lines) are also shown. Prior bounds for ULVZ parameters correspond to the plot widths while those for transition layer parameters are set to ± 1.0 per cent with respect to ak135. (c) Same as (b), but in the case when AR1 parameter is not sampled. (d) Same as (c), but the inversion of ScP-waveform prepared with true ak135 model as background model and the same level of uncorrelated noise is added. (e) Marginals of standard deviation for correlated errors (left), and AR1 parameter (right), prior (shaded), and true values (dashed). Prior bounds are from 0.0 to 0.2 and -0.5 to 0.99 for standard deviation and AR1, and normalized to unit area. Note that uncorrelated noise was added in the ScP waveform.

(http://gji.oxfordjournals.org/lookup/suppl/doi:10.1093/gji/ggv368/-/DC1).

Please note: Oxford University Press is not responsible for the content or functionality of any supporting materials supplied by the authors. Any queries (other than missing material) should be directed to the corresponding author for the paper.